Continuous Remote Sensing Image Super-Resolution based on Context Interaction in Implicit Function Space

Keyan Chen, Wenyuan Li, Sen Lei, Jianqi Chen, Xiaolong Jiang, Zhengxia Zou, and Zhenwei Shi*, *Member, IEEE*

Abstract—Despite its fruitful applications in remote sensing, image super-resolution is troublesome to train and deploy as it handles different resolution magnifications with separate models. Accordingly, we propose a highly-applicable super-resolution framework called FunSR, which settles different magnifications with a unified model by exploiting context interaction within implicit function space. FunSR composes a functional representor, a functional interactor, and a functional parser. Specifically, the representor transforms the low-resolution image from Euclidean space to multi-scale pixel-wise function maps; the interactor enables pixel-wise function expression with global dependencies; and the parser, which is parameterized by the interactor's output, converts the discrete coordinates with additional attributes to RGB values. Extensive experimental results demonstrate that FunSR reports state-of-the-art performance on both fixed-magnification and continuous-magnification settings, meanwhile, it provides many friendly applications thanks to its unified nature.

Index Terms—Remote sensing images, super-resolution, implicit neural network, function space, continuous image representation.

I. INTRODUCTION

IMAGE super-resolution (SR), as a vital technique for elevating image and video spatial resolution, has found vast applications in medical imaging [1, 2], surveillance and security [3, 4], and remote sensing image analysis [5–7], *etc*. Particularly, remote sensing applications including object detection and recognition [8–11], semantic segmentation [12–14], and change detection [15] require high-resolution (HR) images with rich high-frequency details and texture information to perform effective image discrimination, analysis, interpretation, and perception. In face of the forbidden cost in image acquisition, SR becomes indispensable for remote sensing image applications.

Continuous magnification SR is especially vital for remote sensing imagery for three reasons. *First*, imaging real-world surface objects is a process of discretizing continuous signals influenced by the relative acquisition height, so that the objects of the same actual size will show different scales in different images or at different locations. *Second*, multi-source and multi-resolution image processing is the key challenge in remote sensing imagery, which can be partially settled by continuous magnification. *Third*, different spatial resolutions might reveal distinct layers and structures of surface objects. It is also critical to efficiently and effectively run the SR network with different magnifications in various application settings.

Albeit favorable applicability, image SR is hard to achieve due to its ill-posed nature, such that one LR image usually
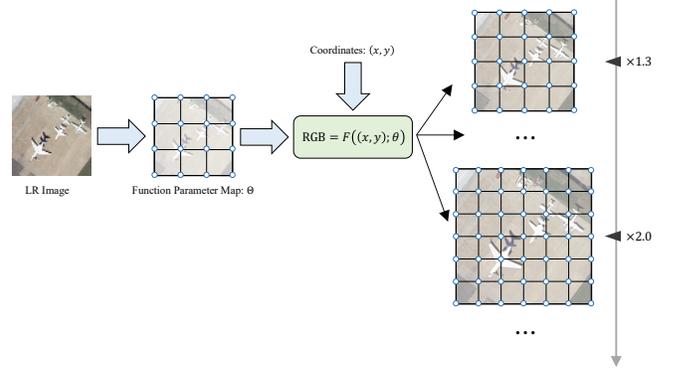

Fig. 1. Our proposed FunSR is capable of producing images of *arbitrary resolution* by *a single trained model*. FunSR converts location coordinates with some additional attributes, *e.g.*, scale factor, to RGB values using functions parameterized by the transformed LR image.

corresponds to a large set of HR ones [16]. To learn this complicated LR-to-HR mapping, compared with classical learning methods or statistical methods based on edge [17, 18], sparse representation [19–21], local information encoding [22, 23], *etc*., deep learning methods demonstrate greater feature expression ability and better performance. Various deep learning methods have been widely employed and achieved milestone results, ranging from the convolutional neural network (CNN) based methods (*e.g.*, [24–27]) to generative adversarial network (GAN) based methods (*e.g.*, [28, 29]) and, more recently, Transformer based methods (*e.g.*, [30, 31]) and implicit neural representation (INR) based methods (*e.g.*, [32, 33]).

Although these methods have greatly improved the development of image SR, the majority of them adhere to the paradigm of using upsampling operations to achieve the enlargement of LR images, and generally only apply a fixed magnification factor or multiple fixed magnification factors. According to the position of the upsampling operation, they may be split into the pre-upsampling SR framework [22, 34] and the post-upsampling one [35, 36]. Most of these methods cannot achieve continuous magnification SR. During the application, they will alter the network structure and retrain the model to meet changing magnification needs, posing significant training, deployment, and storage issues.

Currently, only a few researchers have attempted to use a single model to handle various upscaling factors or continuous factors, and these methods have primarily focused on natural images. These SR methods can be classified into two folds:

conditioned on scale factor and coordinate-based representation. The previous one frequently designs an upsampling module that is conditioned on the scale factor in order to dynamically rescale the output. It is difficult to get optimal performance on out-of-distribution training magnification and large-scale datasets since they simply use a single number (*i.e.*, the magnification) to regulate the continuous spatial resolution. Furthermore, they can only excel in low-magnification (less than ×4) SR conditions. INR-based SR breaks the paradigm of explicitly incorporating the magnification factor as an input, which turns the LR image signal into a representation in the coordinate space, then recovers the HR image by querying the pixel-wise features according to the coordinates. The INR-based SR approach has unique advantages in efficiently modeling continuous differentiable signals and large-scale HR signals. Most INR-based SR methods are extensions of local implicit image function (LIIF) [32], which simply concatenates the coordinates/periodic transformation of coordinates and local features and predicts the RGB value using a multilayer perceptron (MLP) network. These methods mainly focus on synthesis from local representation, ignore global semantic coherence, and miss the expression of multi-level features in diverse magnification settings. Furthermore, concatenating coordinates and local features to the same decoding network limits the representation of local high-frequency details and large-scale datasets.

To address the above concerns, we propose FunSR, a method for learning continuous representations of remote sensing images based on context interaction in implicit function space, as illustrated in Fig. 1. FunSR is made up of three modules: a functional representer, a functional interactor, and a functional parser, as shown in Fig. 2. The functional representor is designed to convert a low-resolution image from Euclidean space into multi-scale pixel-wise function maps, which can be implemented by feature extraction networks, *e.g.*, ResNet [37], EDSR [35], and RDN [38]. The functional interactor allows for the expression of pixel-wise functions with global dependencies, *i.e.*, each local function can interact with any other functions at different locations and levels. It contributes to global semantic coherence within the resulted super-resolved HR images. To fit the image's high-frequency features, the functional parser takes discrete coordinates as input and produces RGB values of the corresponding locations with a periodic activation function [39]. The parameters of the parser are derived from the interactor. We develop a dual-path parser to enhance contextual fusion, *i.e.*, a global parser, and a local parser. The global parser's parameters are shared across locations, whereas the local parser utilizes location-dependent varying parameters.

The main contributions of this paper are as follows:

1) We propose FunSR, a method for learning continuous representations of remote sensing images in implicit function space based on context interaction. FunSR first converts the LR image to a continuous function representation, then takes the HR image's discrete coordinates as input and outputs the RGB values corresponding to the discrete coordinates according to the function. We can achieve arbitrary magnification SR by employing varied sample intervals in the continuous coordinate space.

2) We propose a functional interactor that allows each pixel-wise function to interact with functions at other locations, therefore enhancing global semantic coherence. Furthermore, we present a dual-path functional parser for generating HR images by parsing coordinates from the global and local levels, improving the feature description ability at different concepts.

3) FunSR is a training, deployment, and storage friendly continuous-scale remote sensing image SR framework. It excels at expressing local high-frequency details, contextual consistency, and large-scale signal generalization. In terms of objective indicators and visual effects, FunSR outperforms other state-of-the-art methods.

The remainder of this paper is structured as follows. Sec. II contains a full description of the related works. Sec. III thoroughly discusses the proposed FunSR. Sec. IV presents quantitative and qualitative results as well as ablation studies. Sec. IV brings this paper to a close.

II. RELATED WORKS

A. Deep Learning based Remote Sensing Image SR

Deep learning has made significant progress in the field of remote sensing image SR in recent years [7, 40, 41]. Lei *et al.* [7] propose a local-global-combined network that learns residuals between HR remote sensing images and upscaled LR ones by utilizing the multi-level features of CNN. Qin *et al.* [42] design a gradient-aware loss combined with the L1 loss to improve the recovered edges of surface targets. Wang *et al.* [43] construct a lightweight feature enhancement network to achieve a good trade-off between model complexity and performance for remote sensing images. Chen *et al.* [15] propose a U-Net like network combined with a split attentional fusion model to obtain HR remote sensing images. Moreover, GAN is also introduced to improve the visual super-resolved results for remote sensing LR images. Jiang *et al.* [40] incorporate the edge-enhancement structure into the traditional GAN framework to weaken the influence caused by noises and artifacts. Lei *et al.* [44] propose coupled adversarial training with a well-designed discriminator to learn a better discrimination between the super-resolved image and the corresponding ground truth. Liu *et al.* [45] design a saliency-guided GAN method to improve visual results with additional salient priors. Some researchers focus on the SR of remote sensing satellite videos. Shen *et al.* [46] combine the multi-frame SR model with an edge-guided single-frame SR for remote sensing video reconstruction. These methods are centered on the study of image SR with fixed magnification. In various application scenarios, the network must be redesigned and retrained to accommodate varied magnifications.

B. Image SR with Continuous Magnification

The SR method of arbitrary magnification has significantly advanced research. It vastly outperforms the previous single-magnification SR method in terms of convenience, by breaking the paradigm of just targeting a single specific integer scale. MDSR [35] presents a multi-scale deep SR network with
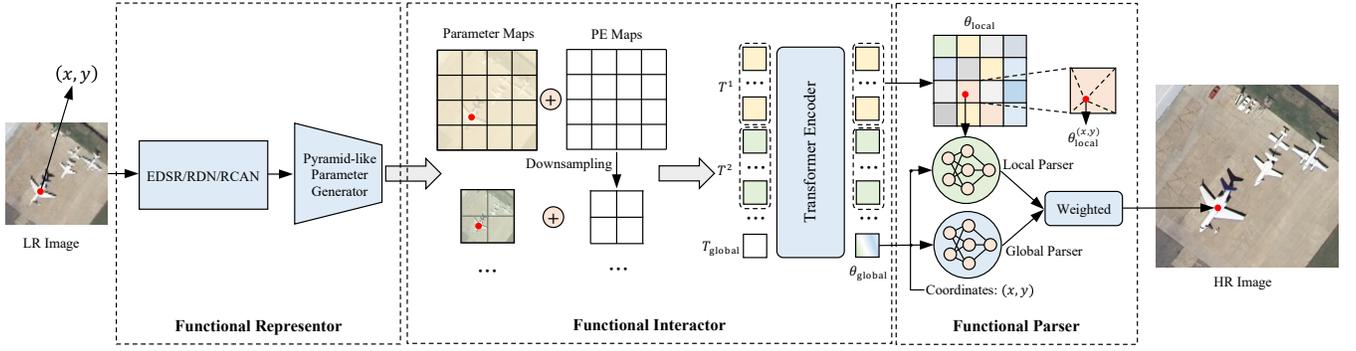
Fig. 2. The outline of the proposed FunSR for continuous magnification remote sensing image SR. The LR image is first converted to multi-scale parameter maps by the functional representor. Then, we design a functional interactor, *i.e.*, a Transformer encoder, to grasp the effective relationship between functions at different pixel-wise locations and contextual levels. It returns a parameter map with global interaction for the local parser and a semantic parameter vector for the global parser via an additional learnable token. Finally, we weight the RGB value produced by the local and global parsers parameterized with the local parameter map and the global parameter vector, respectively, to generate the final RGB value in the HR image.

multiple magnification factors, based on the developed enhanced deep SR network (EDSR) in the paper, but it can only deal with several pre-defined integer magnifications. Meta-SR [47] achieves SR at arbitrary magnification by the designed meta-upscale module, which can utilize the coordinates and scale factors to build the parameters of the convolution kernel. However, using a single simple scale information to condition the entire SR network would restrict the performance. The architecture of Meta-SR has been further explored and improved in some subsequent works (*e.g.*, ArbRCAN [48], RSI-HFAS [49], RSAN [50]). They often design a scale parser module to term the magnification factor as a network conditional input, or an upsampling module to dynamically resize the feature map according to the magnification. These methods use a single variable (magnification factor) to dynamically modulate the spatial size of the SR image. It is difficult to attain optimal performance in out-of-distribution and large-scale synthesis [32], and these methods still focus on the synthesis of low-upscale factor (less than $\times 4$).

C. Implicit Neural Representations

INR enables continuous magnification image SR by breaking the paradigm of explicitly employing magnification factors as network input. It can recover high-quality SR images of any size by learning continuous image representation in coordinate space and then sampling discrete pixel signals based on different-sized coordinate maps. INR is essentially a continuously differentiable function that can map properties (*e.g.*, amplitude, intensity, distance) of a space/time point as a function of the related coordinates, *i.e.*, $F_{\theta} : \mathbb{R}^n \rightarrow \mathbb{R}^m$. Taking representing an image as an example, F_{θ}, usually an MLP, converts coordinates ($n = 2$, the coordinates) to pixel values ($m = 3$, RGB values). It is extensively used to represent objects, images, scenes, *etc*. Learning implicit neural representations of 2D images lends itself well to image super-resolution challenges, where more detailed (*i.e.*, higher resolution) image representations can be acquired by sampling pixel signals (*i.e.*, RGB values) anywhere in the spatial domain. Inspired by INR, LIIF [32] designs a local implicit image function to achieve continuous image SR, which takes the coordinates and nearby

feature representations as input and outputs the RGB value of the corresponding location. Based on LIIF, IPE-LIIF [51] aggregates local frequency information by positional encoding to improve SR performance. UltraSR [33] deeply integrates coordinate encoding with implicit neural representations to improve the accuracy of high-frequency textures.

The aforementioned INR-based SR methods concentrate on constructing an upsampling decoding module by simply concatenating the coordinates/periodic encodings of coordinates and local features together, and predicting the RGB value of the corresponding location using an MLP network. These methods ignore global semantic consistency and multi-level feature expression at different magnification scenarios. Furthermore, merely concatenating coordinates and local features to the same decoding network will limit the expression of local high-frequency details and large-scale image data while also having an effect on generalization. These limitations have a greater impact on SR performance for remote sensing image data, since they have a more complicated distribution, richer details and textures, and a larger data scale than SR datasets frequently utilized in natural images, *e.g.*, face. To alleviate the aforementioned challenges, we propose FunSR, which transforms the LR image from the image's Euclidean space to the function space, performs multi-scale and global interaction in the function space, and uses local and global functional parsers to get the function value (*i.e.*, RGB value) of the HR image.

D. Transformer for Image Processing

Transformer was originally developed in natural language processing [52]. Thanks to its capacity to build long-distance dependencies, researchers have steadily adapted Transformer to computer vision applications in recent years and achieved tremendous success. ViT [53] verifies that directly applying a pure transformer to sequences of image patches can reach the bar on the performance of a CNN-based model on image classification tasks. DETR [54] builds a CNN-Transformer hybrid fully end-to-end detector by combining the benefits of CNN and transformer without anchor generation and non-maximum suppression post-processing. TTSR [30] introduces

a novel texture Transformer network for image SR, in which low- and high-resolution images are formulated as queries and keys in a transformer, respectively. TransENet [41] proposes a transformer-based enhancement network for remote sensing image SR by exploiting features at various levels. Our proposed FunSR intends to leverage Transformer to enhance the interaction between functions at different spatial locations and different conceptual levels.

III. METHODOLOGY

In this section, we will introduce the proposed FunSR, a continuous SR method for remote sensing images, including the overview, functional representor, functional interactor, functional parser, and loss function.

A. Overview

The outline of the proposed FunSR is shown in Fig. 2. Assume we are given a training dataset, *i.e.*, $\mathcal{D}_{\text{train}} = \{(\mathcal{I}_{\text{LR}}^1, \mathcal{I}_{\text{HR}}^1), \ldots, (\mathcal{I}_{\text{LR}}^N, \mathcal{I}_{\text{HR}}^N)\}$, where $\mathcal{I}_{\text{LR}}^i \in \mathbb{R}^{H \times W \times 3}$ and $\mathcal{I}_{\text{HR}}^i \in \mathbb{R}^{H' \times W' \times 3}$ refer to the original LR image and its corresponding ground-truth HR reference. Our goal is to train a model that can process any image from a test set ($\mathcal{I}_{\text{LR}}^k \sim \mathcal{D}_{\text{test}}$), simultaneously obtaining various magnification HR images through coordinate maps of different sizes as follows,

$$\Theta = \Phi_{\text{interactor}} \circ \Phi_{\text{representor}}(\mathcal{I}_{\text{LR}}^k)$$
$$\mathcal{I}_{\text{HR}} = \Phi_{\text{parser}}((x_i, y_i); \Theta) \tag{1}$$

where the image is processed progressively by a functional representor and a functional interactor to generate the local-global interacted parameter map ($\Theta \in \mathbb{R}^{H \times W \times d}$) of the function. By inputting the discrete coordinates ($(x_i, y_i) \sim \{(x_0, y_0), (x_1, y_1), \cdots\}$) to the functions ($\Phi_{\text{parser}}$ with parameters Θ), we can acquire the RGB value corresponding to the location (x_i, y_i). Considering that we use different intervals on continuous coordinates to sample discrete coordinate maps of different sizes, we can obtain HR images of different magnifications through a unified function parser. For simplicity, we will omit the superscript k when describing the proposed model.

B. Functional Representor

The functional representor is designed to transform LR images of Euclidean space to function space parameters like follows:

$$\mathcal{M} = \{\theta^1, \cdots, \theta^l\} = \Phi_{\text{representor}}(\mathcal{I}_{\text{LR}})$$
$$= \Phi_{\text{pyramid}} \circ \Phi_{\text{encoder}}(\mathcal{I}_{\text{LR}}) \tag{2}$$

where θ^i refers to the parameter map at the i-th level. The encoder (Φ_{encoder}) used in our method is a CNN module without any upscaling layer. We have adopted some modules in previous works as the encoder directly, including EDSR [35], RCAN [55], and RDN [38]. In order to allow pixel-level functions to resolve local visual representations at multiple scales and levels, we design a pyramid-like parameter generator (Φ_{pyramid}). For simplicity and efficiency, the structure of
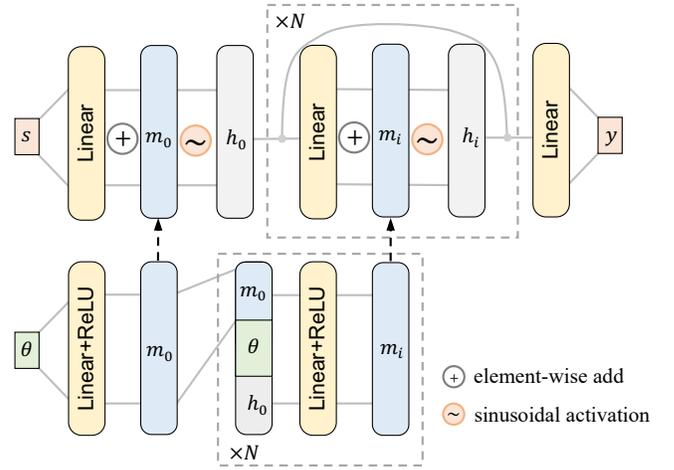

Fig. 3. An illustration of the proposed functional parser, an N-layer MLP with a sinusoidal activation function. It takes coordinates with some additional attributes as input (s), and returns RGB values (y). The parser's parameters are modulated by θ.

Φ_{pyramid} follows a downsampling pipeline rather than an upsampling one, based on Cross Stage Partial Layer (CSPLayer) [56, 57]. We use three CSPLayers with a downsampling factor of 2 between each layer, which generates four parameter maps of different sizes, *i.e.*, $\mathcal{M} = \{\theta^i \in \mathbb{R}^{\frac{H}{2^{i-1}} \times \frac{W}{2^{i-1}} \times d}\}, i \in \{1, 2, 3, 4\}$.

C. Functional Interactor

We present a functional interactor to enable the expression of local pixel-wise functions to imply global information, *i.e.*, to allow each local pixel-wise function to interact with functions at other locations, even at different conceptual levels. The functional interactor contributes to the global semantic coherence of the final parsed HR image. Here, we use self-attention based Transformer encoder layers [52] to implement the interaction between multi-level local functions as follows,

$$T^i = \text{Flatten}(\theta^i + \Phi_{\text{samp}}(PE))$$
$$T = \text{Cat}([T_{\text{global}}, T^1, \cdots, T^l])$$
$$\Theta = \{\theta_{\text{global}}, \theta_{\text{local}}\} \tag{3}$$
$$= \Phi_{\text{interactor}}(\mathcal{M}) = \Phi_{\text{transformer}}(T)$$

where $PE \in \mathbb{R}^{H \times W \times d}$ is a learnable positional encoding map with the same shape as the first level parameter map, θ^1. Φ_{samp} denotes bicubic sampling, making it possible to use the same positional encoding map for other size parameter maps. Flatten is an operation to flatten the map to vectorized tokens (T^i). T_{global} is a learnable token used to capture global information for subsequent global parsing. Cat represents vector concatenation to increase the token number. The functional interactor uses N-layer plain transformer encoders ($\Phi_{\text{transformer}}$) to establish dependencies between local functions at different levels, and finally obtains functional parameters that can express global semantic content: global function parameter vector ($\theta_{\text{global}} \in \mathbb{R}^{1 \times d}$) from the first token of the output; local pixel-level function parameter map ($\theta_{\text{local}} \in \mathbb{R}^{H \times W \times d}$) reshaping from the 2-nd to $(H \times W + 1)$-th token of the output.

D. Dual-path Parser

Through the functional representor ($\Phi_{\text{representor}}$) and the functional interactor ($\Phi_{\text{interactor}}$), we can represent the LR image as the parameters (Θ) of functions. A naive idea is that these parameters reflect the mapping relationship between image coordinates (x_i, y_i) and image pixel values $\mathcal{I}_{(x_i,y_i)}$, *i.e.*, $\mathcal{I}_{(x_i,y_i)} = f_\Theta(x_i, y_i)$. We view this as a parsing process from coordinates to pixel values, *i.e.*, term f_Θ as a functional parser (Φ_{parser}), as illustrated in Eq. 1. Considering that we use different sampling intervals of a fixed range, generally $[-1, 1]$, we can obtain coordinate maps of different sizes. Using the functions to parse these coordinates to retrieve the corresponding pixel values, we can generate HR images of any sizes, and achieve continuous magnification SR. Furthermore, the coordinate-based representation method allows us to easily obtain SR of out-of-distribution magnifications.

We present a dual-path coordinate parser that can parse coordinates from both the global and local perspectives, as well as improve image feature descriptions at various levels. The difference between the two parsers is that: the parameters of the global parser are shared across spatial positions; the parameters of the local parser are dependent on the spatial location. The formula description is given below,

$$
\begin{aligned}
\mathcal{I}_{\text{global}} &= \Phi_{\text{global}}((x_i, y_i); \theta_{\text{global}}) \\
\theta_{\text{local}}^{(x_i,y_i)} &= \Phi_{\text{interp}}(\theta_{\text{local}}, (x_i, y_i)) \\
\mathcal{I}_{\text{local}} &= \Phi_{\text{local}}((x_i, y_i); \theta_{\text{local}}^{(x_i,y_i)}) \\
\hat{\mathcal{I}}_{\text{HR}} &= \text{Conv}(\text{Cat}([\mathcal{I}_{\text{global}}, \mathcal{I}_{\text{local}}]))
\end{aligned}
\tag{4}
$$

where (x_i, y_i) is the coordinate, Φ_{global} and Φ_{local} are the two parsers respectively, and Φ_{interp} is an interpolation operation to get the local function parameters at an arbitrary location, *i.e.*, $\theta_{\text{local}}^{(x_i,y_i)} \in \mathbb{R}^{1 \times d}$ from the local parameter map (θ_{local}). We utilize the nearest interpolation to obtain the local function parameters of a query location for efficiency. $\mathcal{I}_{\text{global}}$ and $\mathcal{I}_{\text{local}}$ are the plain HR images parsed from the global and local parsers respectively. To produce the required RGB image, we simply concatenate the two to form a 6-channel image and use a convolutional layer with a kernel size of 3 to restore the 3-channel HR image.

Following that, we will go over Φ_{global} and Φ_{local} in further detail. They are identical in network architecture, so we will introduce the global parser as an example. When representing pixel values as a function of coordinates, the first challenge lies in the difficulty to use neural networks to fit high-frequency features of images, *e.g.*, edges, and textures. Fortunately, previous studies have explored the Fourier feature mapping [58, 59] and periodic activation functions [39, 60] to learn high-frequency functions in low-dimensional domains. We employ a similar MLP architecture with periodic activation functions to form the parser, also known as Sirens [39, 60]. If the parser's parameters are entirely sourced from θ_{global}, the training of FunSR will suffer from the θ_{global} with very high dimension. It's also resource-intensive work.

As a result, we only use θ_{global} as part of the parser's parameters to regulate the frequency and phase of the periodic activation functions. In this way, only a small number of
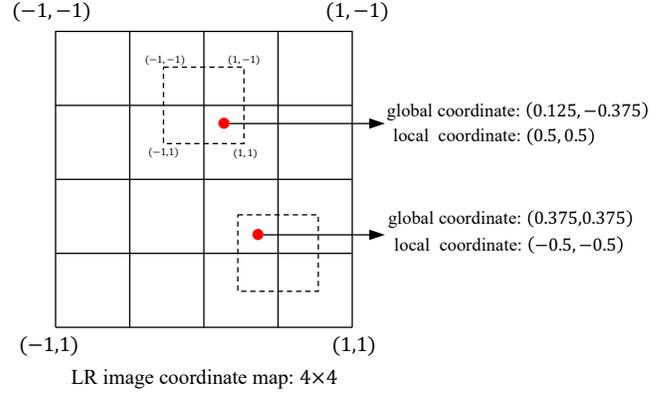

Fig. 4. The global and local coordinates are supposed to be relative to the center of the image and the center of the nearest LR pixel, respectively. All are rescaled to $[-1, 1]^2$.

parameters (*e.g.*, as few as 64) can be used to perfectly control the whole parsing process, which is friendly for training. Our parser performs an N-layer MLP, as illustrated in Fig. 3, which can be written recursively as follows,

$$
\begin{aligned}
m_0 &= \text{ReLU}(w_0^m \theta_{\text{global}} + b_0^m) \\
h_0 &= \sin(w_0^h s + m_0) \\
m_i &= \text{ReLU}(w_i^m \text{Cat}([\theta_{\text{global}}, m_{i-1}, h_{i-1}]) + b_i^m) \\
h_i &= \sin(w_i^h h_{i-1} + m_i) + h_{i-1} \\
y &= w_N^h h_{N-1} + b_N^h
\end{aligned}
\tag{5}
$$

where w_i^m, w_i^h, b_i^m, and b_i^h are the weights and biases, i indicates the i-th layer, and s is the input global coordinates (x_i, y_i) with some additional attributes, *e.g.*, scale factor, interpolated RGB value, and local coordinates (here, we refer to the global and local coordinates relative to the center of the image and the center of the nearest LR pixel respectively, as shown in Fig. 4). m_i denotes the bias shift to regulate the frequency and phase of the sinusoidal activation function. h_i is the intermediate state of the parser. Cat means vector concatenation. The first two formulas describe the modeling process of the first MLP layer, the last one represents the output of the final pixel values of the HR image, and the other two represent the MLP's middle layers.

E. Loss Function

We train the proposed model using the L1 loss function with $\mathcal{D}_{\text{train}}$ as shown bellow,

$$
\mathcal{L} = \frac{1}{N \cdot M} \sum_{i=0}^{N} \sum_{j=0}^{M} \| \hat{\mathcal{I}}_{\text{HR}}^{(x_i,y_j)} - \mathcal{I}_{\text{HR}}^{(x_i,y_j)} \|_1
\tag{6}
$$

here, we just show the loss function for an image. $\hat{\mathcal{I}}_{\text{HR}}$ and $\mathcal{I}_{\text{HR}}$ are the HR images from our proposed FunSR model and annotations, respectively. (x_i, y_j) is the sampling location for supervised training. N and M denote the width and height of the image.

IV. EXPERIMENTAL RESULTS AND ANALYSES

A. Experimental Dataset and Settings

In this paper, we use two public remote sensing datasets, UCMecred [61] and AID [62], to verify the effectiveness of the proposed method. These datasets have been widely used in the field of remote sensing SR [7, 36, 41].

UCMecred Dataset [61]: This dataset covers 21 different types of remote sensing scenarios, *e.g.*, agricultural, airplane, baseball diamond, and beach. There are 100 images in each class with a size of 256×256 pixels, and a spatial resolution of 0.3 m/pixel. We split the dataset into a training set, a validation set, and a test set with a ratio of 6:2:2 for each class.

AID Dataset [62]: This dataset contains 10000 images from 30 different remote sensing scenes, *e.g.*, airport, bareland, church, and dense-residential. All images have an image resolution of 600×600 pixels and a spatial resolution of 0.5 m/pixel. For the AID dataset, 80% of the images in each class are selected at random to represent the training set, while the remaining images serve as the test set. Furthermore, we randomly choose 10 images per class in a total of 300 images to form the corresponding validation dataset.

B. Evaluation Protocol and Metrics

To evaluate the performance of the proposed method, we take two most popular metrics: Peak Signal-to-Noise Ratio (PSNR) and Structural SIMilarity (SSIM). They are commonly used to objectively assess the quality of image reconstruction [41, 63]. PSNR is defined by Mean Squared Error (MSE), as follows,

$$\text{PSNR} = 10 \times \log_{10} \left(\frac{\text{L}^2}{\text{MSE}} \right) \tag{7}$$

where L denotes the achievable largest pixel value, *e.g.*, 255 for an 8-bit image.

SSIM is more concerned with the perceptual quality of two images, as demonstrated by,

$$\begin{aligned} \text{SSIM} &= [l(x,y)]^\alpha \cdot [c(x,y)]^\beta \cdot [s(x,y)]^\gamma \\ l(x,y) &= \frac{2\mu_x\mu_y + C_1}{\mu_x^2 + \mu_y^2 + C_1} \\ c(x,y) &= \frac{2\sigma_x\sigma_y + C_2}{\sigma_x^2 + \sigma_y^2 + C_2} \\ s(x,y) &= \frac{\sigma_{xy} + C_3}{\sigma_x\sigma_y + C_3} \end{aligned} \tag{8}$$

where $l(x,y)$, $c(x,y)$ and $s(x,y)$ are measures of luminance, contrast, and structure, respectively, μ_x and μ_y are the mean value of x and y. σ_x and σ_y are the variance of x and y, σ_{xy} is the covariance of x and y. C_1, C_2 and C_3 are constants. α, β and γ are usually set to 1.

C. Implementation Details

This method focuses on learning continuous representation for remote sensing image SR, *i.e.*, remote sensing image SR with continuous magnifications. In our experiments, we consider the original image to be a real HR reference, and the corresponding LR image is produced via bicubic downsampling.

1) Architecture Details: For the functional representor, we utilize EDSR [35], RCAN [55], and RDN [38], without their upsampling module, as the encoder in our experiments. The pyramid-like parameter generator is formed by a 3-layer CSPLayer module with 2, 4, and 6 Darknet Bottleneck blocks in each CSPLayer. The functional interactor is a 3-layer transformer encoder with 256 input and output dimensions and 512 feedforward dimensions. As for the parser, the global and local parsers use the same design, but with distinct parameter modulations. Specifically, the functional parser is made up of a 5-layer MLP (each with 256 hidden units), as described in Sec. III-D.

2) Training Details: During the training phase, 48×48 patches are randomly cropped from LR remote sensing images, and reference patches are cropped from their corresponding HR ones. Meanwhile, we use random rotation ($90°$, $180°$, and $270°$) and horizontal flipping to augment the training samples. The coordinate and image RGB values are all normalized to be between -1 and 1. The scale factors in the training phase are uniformly distributed from 1 to 4. During the test phase, the LR test images are cropped into a set of 48×48 patches and then fed into the model without any bells and whistles.

For optimization, we use AdamW optimizer with an initial learning rate of $1e-4$ to train our model. The mini-batch size is set to 8. The total training epochs are 4000 for the UCMecred dataset and 2000 for the AID dataset. We conduct a Cosine Annealing scheduler [70] to decay the learning rate. The proposed method is implemented by PyTorch, and all experiments are run on an NVIDIA A100 Tensor Core GPU.

D. Comparison with the State-of-the-Art

In this section, we compare the proposed method with some other state-of-the-art SR methods, including the classic bicubic interpolation, fixed magnification SR methods (*e.g.*, SRCNN [64], FSRCNN [65], LGCNet [7], VDSR [34], DCM [36], TransENet [41]), and continuous magnification SR methods (*e.g.*, MetaSR [47], LIIF [32], A-LIIF [67], DIINN [68], SADN [69], OverNet [66], ArbRCAN [48]). In terms of continuous magnification image SR, we have applied various image encoders (EDSR [35], RCAN [55], and RDN [38]) to verify the robustness of the proposed method. We can run out-of-distribution evaluations (training under $\times 4$, evaluating beyond $\times 4$) because of the coordinate-based architecture. All the methods are implemented according to the official publications with Pytorch.

1) Quantitative Results on the UCMerced Dataset: The results of FunSR versus other comparison methods on the UCMerced Dataset are shown in Tab. I, with the best performance shown by a bold number. We just show the upscale factor of $\times 2.0$, $\times 2.5$, $\times 3.0$, $\times 3.5$, $\times 4.0$, $\times 6.0$, $\times 8.0$, and $\times 10.0$ for simplicity. FunSR nearly achieves the highest performance in terms of PSNR and SSIM across all backbones and upscale factors. Specifically, FunSR outperforms the state-of-the-art fixed magnification transformer-based SR method TransENet (26.98/0.7755) by 27.11/0.7781, 27.24/0.7799, and 27.29/0.7798 on PSNR and SSIM under $\times 4$ magnification utilizing EDSR, RCAN, and RDN image encoders, respectively. FunSR has also shown comparable performance with

TABLE I
MEAN PSNR (DB) AND SSIM ON THE UCMERCED TEST DATASET WITH CONTINUOUS UPSCALE FACTORS.

Method		In-distribution (PSNR↑/SSIM↑)					Out-of-distribution (PSNR↑/SSIM↑)		
		×2.0	×2.5	×3.0	×3.5	×4.0	×6.0	×8.0	×10.0
Bicubic		31.96/0.9029	28.77/0.8356	26.68/0.7698	25.48/0.7228	24.55/0.6803	22.04/0.5597	20.74/0.4926	19.85/0.4527
SRCNN [64]		32.71/0.9094	-	27.14/0.7824	-	25.15/0.6984	-	-	-
FSRCNN [65]		32.04/0.8988	-	26.94/0.7756	-	24.92/0.6913	-	-	-
LGCNet [7]		33.48/0.9196	-	27.36/0.7913	-	25.33/0.7108	-	-	-
VDSR [34]		33.97/0.9254	-	28.08/0.8126	-	25.90/0.7364	-	-	-
DCM [36]		34.01/0.9263	-	28.20/0.8156	-	26.02/0.7414	-	-	-
TransENet [41]		33.78/0.9233	-	28.87/0.8322	-	26.98/0.7755	-	-	-
OverNet [66]		33.89/0.9243	30.43/0.8675	28.23/0.8142	27.05/0.7770	26.05/0.7412	22.98/0.6017	21.34/0.5186	20.24/0.4667
MetaSR [47]	EDSR	32.31/0.9066	29.25/0.8439	27.16/0.7832	26.06/0.7404	25.14/0.7008	22.62/0.5800	21.32/0.5122	20.47/0.4720
LIIF [32]	EDSR	33.91/0.9242	30.59/0.8700	28.42/0.8178	27.33/0.7862	26.32/0.7487	23.33/0.6204	21.82/0.5472	20.79/0.5001
A-LIIF [67]	EDSR	33.78/0.9224	30.53/0.8690	28.36/0.8158	27.27/0.7841	26.28/0.7469	23.32/0.6191	21.83/0.5469	20.84/0.5015
DIINN [68]	EDSR	34.32/0.9292	31.00/0.8793	28.79/0.8281	27.70/0.7994	26.64/0.7637	23.42/0.6259	21.88/0.5510	20.82/**0.5017**
SADN [69]	EDSR	34.18/0.9278	30.87/0.8772	28.64/0.8250	27.53/0.7931	26.50/0.7575	23.31/0.6223	21.73/0.5450	20.71/0.4985
FunSR	EDSR	**34.61/0.9318**	**31.40/0.8860**	**29.19/0.8391**	**28.10/0.8095**	**27.11/0.7781**	**23.62/0.6314**	**22.05/0.5531**	**20.98**/0.5007
MetaSR [47]	RCAN	33.89/0.9227	30.59/0.8702	28.40/0.8166	27.31/0.7849	26.33/0.7482	23.26/0.6162	21.48/0.5328	20.36/0.4808
LIIF [32]	RCAN	34.27/0.9282	31.02/0.8792	28.92/0.8336	27.81/0.8008	26.83/0.7682	23.54/0.6322	21.79/0.5516	20.54/0.4956
A-LIIF [67]	RCAN	34.18/0.9268	30.94/0.8775	28.82/0.8305	27.71/0.7972	26.72/0.7625	23.47/0.6302	21.86/0.5539	20.77/0.5002
DIINN [68]	RCAN	34.71/0.9323	31.47/0.8871	29.33/0.8430	28.20/0.8124	27.16/0.7792	23.44/0.6300	21.54/0.5408	20.38/0.4872
ArbRCAN [48]	RCAN	34.72/0.9328	31.39/0.8866	29.20/0.8393	28.10/0.8089	27.10/0.7772	23.24/0.6116	21.48/0.5256	20.42/0.4746
FunSR	RCAN	**34.86/0.9341**	**31.65/0.8902**	**29.41/0.8445**	**28.27/0.8156**	**27.24/0.7799**	**23.65/0.6341**	**21.94/0.5553**	**20.81/0.5010**
MetaSR [47]	RDN	34.23/0.9263	30.98/0.8778	28.83/0.8295	27.73/0.7980	26.76/0.7654	23.55/0.6309	21.83/0.5481	20.66/0.4945
LIIF [32]	RDN	34.30/0.9277	31.07/0.8801	28.94/0.8336	27.84/0.8021	26.88/0.7676	23.63/0.6364	21.95/0.5569	20.78/**0.5040**
A-LIIF [67]	RDN	34.19/0.9274	30.96/0.8781	28.81/0.8288	27.68/0.7960	26.72/0.7615	23.56/0.6337	21.91/0.5548	20.79/0.5034
DIINN [68]	RDN	34.68/0.9322	31.38/0.8851	29.26/0.8405	28.11/0.8094	27.06/0.7744	23.55/0.6361	21.90/0.5548	20.78/0.5029
SADN [69]	RDN	34.57/0.9312	31.31/0.8840	29.09/0.8338	28.01/0.8051	26.98/0.7712	23.46/0.6329	21.67/0.5453	20.65/0.5000
FunSR	RDN	**34.82/0.9341**	**31.64/0.8898**	**29.41/0.8416**	**28.31/0.8113**	**27.29/0.7798**	**23.69/0.6372**	**22.04/0.5575**	**20.93**/0.5038

TABLE II
MEAN PSNR (DB) AND SSIM ON THE AID TEST DATASET WITH CONTINUOUS UPSCALE FACTORS.

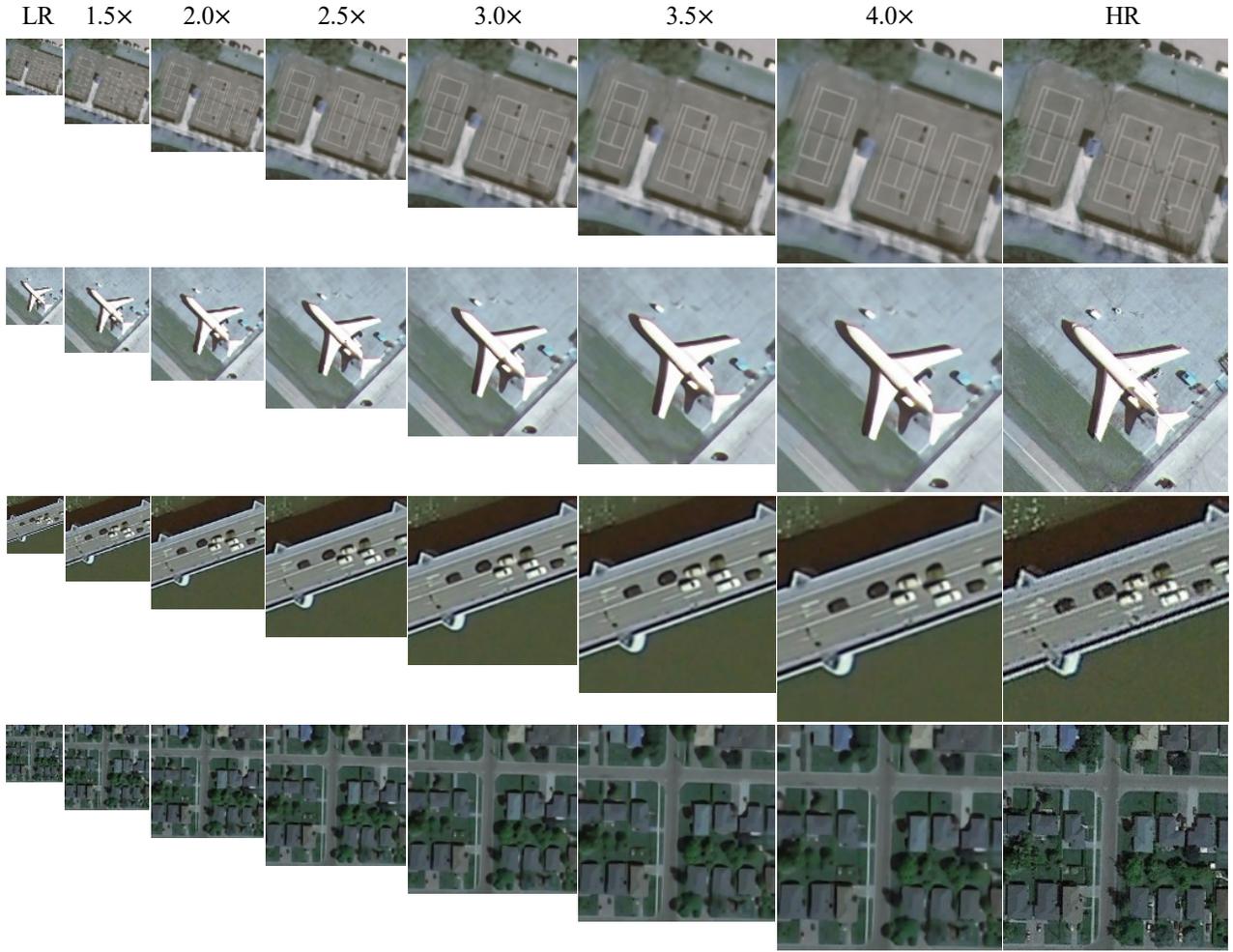| Method		In-distribution (PSNR↑/SSIM↑)					Out-of-distribution (PSNR↑/SSIM↑)		
		×2.0	×2.5	×3.0	×3.5	×4.0	×6.0	×8.0	×10.0
Bicubic		34.93/0.9169	31.76/0.8560	29.69/0.7995	28.45/0.7595	27.48/0.7245	24.66/0.6207	23.15/0.5656	22.15/0.5302
SRCNN [64]		35.70/0.9245	-	30.31/0.8151	-	28.21/0.7465	-	-	-
FSRCNN [65]		35.10/0.9177	-	29.93/0.8051	-	28.06/0.7416	-	-	-
LGCNet [7]		36.17/0.9304	-	30.59/0.8231	-	28.45/0.7563	-	-	-
VDSR [34]		36.46/0.9341	-	31.01/0.8350	-	28.93/0.7743	-	-	-
DCM [36]		36.55/0.9352	-	31.19/0.8396	-	29.14/0.7804	-	-	-
TransENet [41]		36.56/0.9357	-	31.43/0.8467	-	29.47/0.7937	-	-	-
OverNet [66]		36.54/0.9354	33.31/0.8875	31.32/0.8435	30.21/0.8127	29.26/0.7850	26.21/0.6814	24.49/0.6102	23.35/0.5601
MetaSR [47]	EDSR	36.35/0.9326	33.15/0.8841	31.17/0.8391	30.06/0.8074	29.11/0.7790	26.18/0.6814	24.54/0.6182	23.44/0.5730
LIIF [32]	EDSR	36.47/0.9346	33.27/0.8869	31.29/0.8429	30.20/0.8122	29.25/0.7847	26.33/0.6895	24.67/0.6274	**23.55**/0.5824
A-LIIF [67]	EDSR	36.43/0.9340	33.23/0.8860	31.24/0.8415	30.14/0.8103	29.19/0.7825	26.29/0.6875	24.64/0.6262	23.53/0.5818
DIINN [68]	EDSR	36.65/0.9366	33.40/0.8895	31.42/0.8461	30.33/0.8160	29.37/0.7891	26.36/0.6933	24.63/0.6290	23.47/**0.5825**
SADN [69]	EDSR	36.61/0.9363	33.39/0.8892	31.40/0.8455	30.30/0.8153	29.36/0.7885	26.36/0.6918	24.64/0.6277	23.52/0.5823
FunSR	EDSR	**36.74/0.9382**	**33.49/0.8925**	**31.53/0.8499**	**30.44/0.8205**	**29.51/0.7948**	**26.46/0.6969**	**24.72/0.6298**	23.53/0.5816
MetaSR [47]	RCAN	36.75/0.9373	33.51/0.8918	31.54/0.8496	30.46/0.8202	29.54/0.7942	26.59/0.7008	24.87/0.6359	23.70/0.5874
LIIF [32]	RCAN	36.80/0.9383	33.57/0.8930	31.60/0.8511	30.53/0.8219	29.61/0.7962	26.68/0.7046	24.98/0.6419	**23.81**/0.5942
A-LIIF [67]	RCAN	36.78/0.9382	33.55/0.8926	31.58/0.8505	30.52/0.8216	29.59/0.7960	26.66/0.7039	24.96/0.6415	23.79/**0.5943**
DIINN [68]	RCAN	36.97/0.9400	33.70/0.8952	31.71/0.8535	30.63/0.8247	29.70/0.7993	26.68/0.7059	24.91/0.6408	23.70/0.5920
ArbRCAN [48]	RCAN	37.11/0.9410	33.83/0.8969	31.78/0.8548	30.66/0.8255	29.72/0.8001	26.44/0.6943	24.57/0.6179	23.38/0.5652
FunSR	RCAN	**37.16/0.9417**	**33.86/0.8982**	**31.82/0.8554**	**30.73/0.8272**	**29.83/0.8017**	**26.75/0.7063**	**25.03/0.6427**	23.79/0.5938
MetaSR [47]	RDN	36.77/0.9374	33.52/0.8917	31.55/0.8497	30.48/0.8204	29.56/0.7943	26.62/0.7017	24.90/0.6373	23.72/0.5886
LIIF [32]	RDN	36.81/0.9382	33.57/0.8927	31.60/0.8505	30.52/0.8215	29.60/0.7957	26.68/0.7039	24.98/0.6414	**23.80/0.5939**
A-LIIF [67]	RDN	36.76/0.9379	33.51/0.8917	31.55/0.8496	30.48/0.8203	29.55/0.7944	26.63/0.7022	24.93/0.6397	23.76/0.5927
DIINN [68]	RDN	36.98/0.9398	33.71/0.8950	31.71/0.8533	30.62/0.8243	29.68/0.7987	26.65/0.7042	24.88/0.6387	23.68/0.5899
SADN [69]	RDN	36.84/0.9386	33.58/0.8930	31.60/0.8507	30.53/0.8217	29.60/0.7961	26.56/0.7016	24.81/0.6367	23.63/0.5890
FunSR	RDN	**37.01/0.9406**	**33.79/0.8968**	**31.81/0.8557**	**30.73/0.8269**	**29.82/0.8018**	**26.70/0.7043**	**25.01/0.6417**	23.77/0.5923

Fig. 5. The visual comparisons of some image examples upsampling with different scale factors by FunSR-RDN. The LR image is downsampled from the HR reference image with a scale ratio of $1/4$. The first two rows are from the UCMerced test set ("tenniscourt99" and "airplane35"), while the last two are from the AID test set ("bridge_28" and "denseresidential_20").
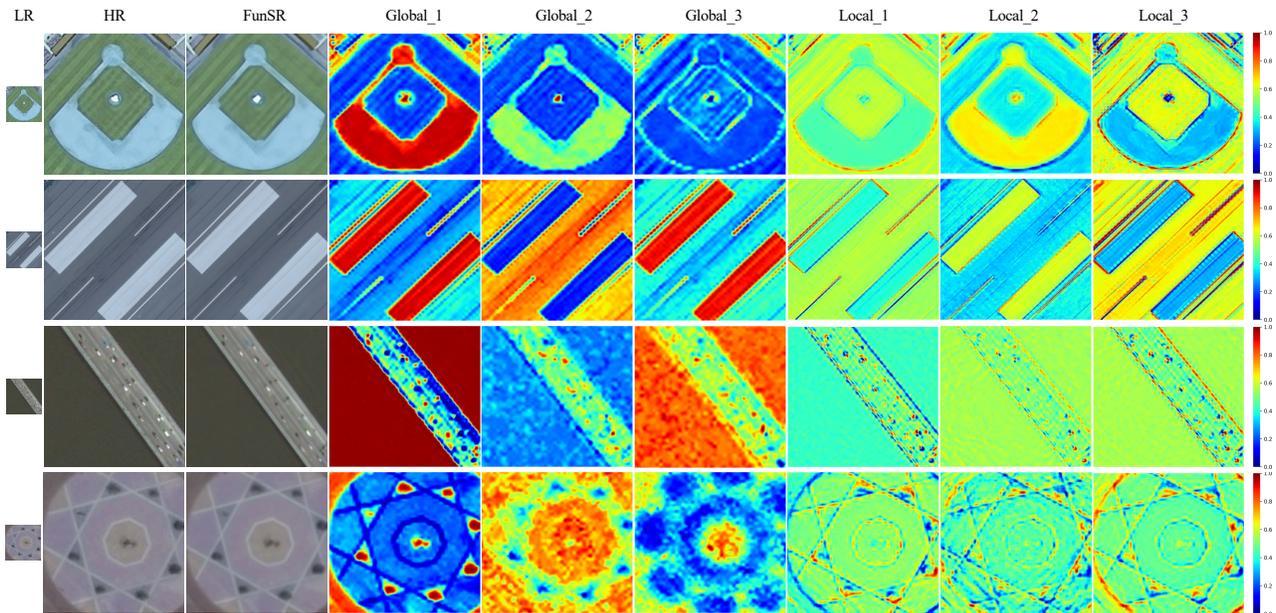

Fig. 6. Some visual examples of the feature maps generated from the global and local parsers with an upscale factor of $\times 4$. The first two rows are scenes ("baseballdiamond31" and "runway76") from the UCMerced dataset and the last two rows ("bridge_353" and "square_83") are from the AID dataset.
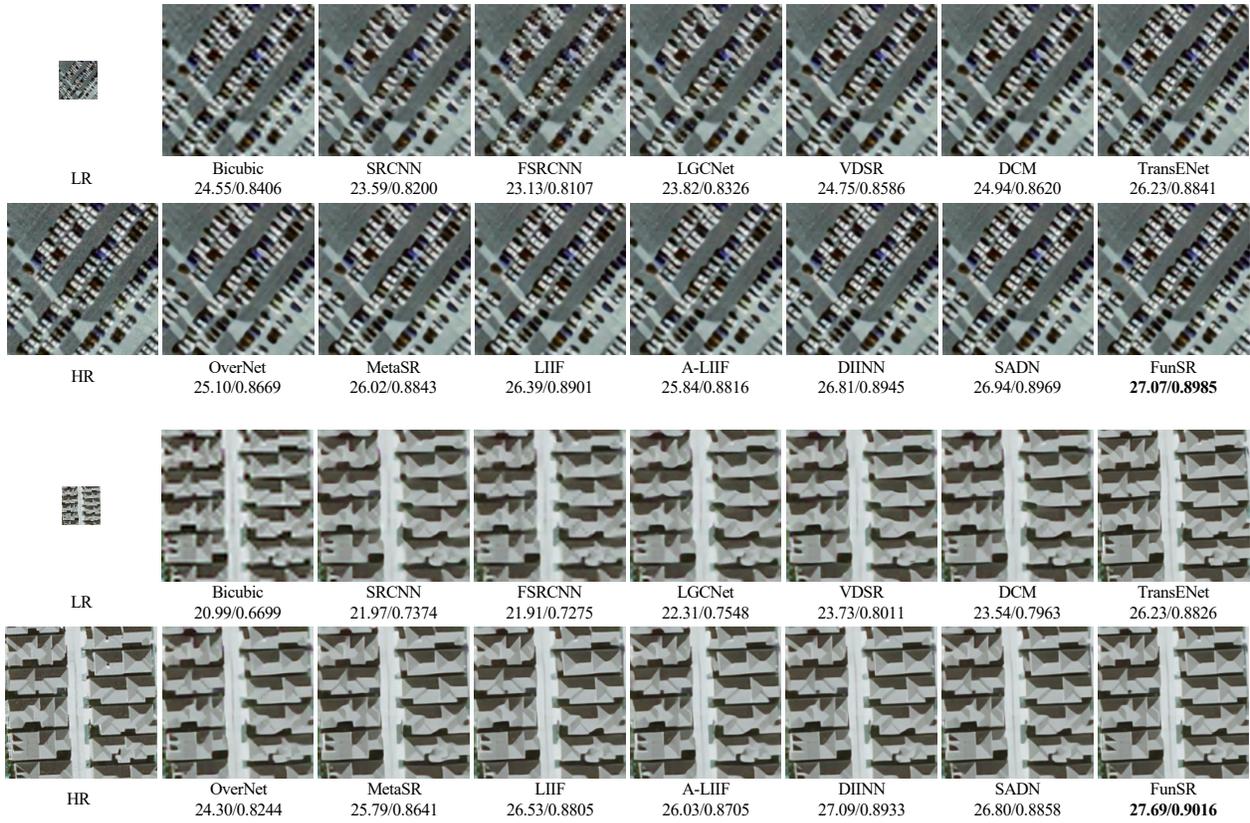
Fig. 7. Comparisons on the UCMerced test set with different methods under ×4 factor. Image crops are from "parkinglot17" and "denseresidential58" respectively. Zoom in for better visualization.

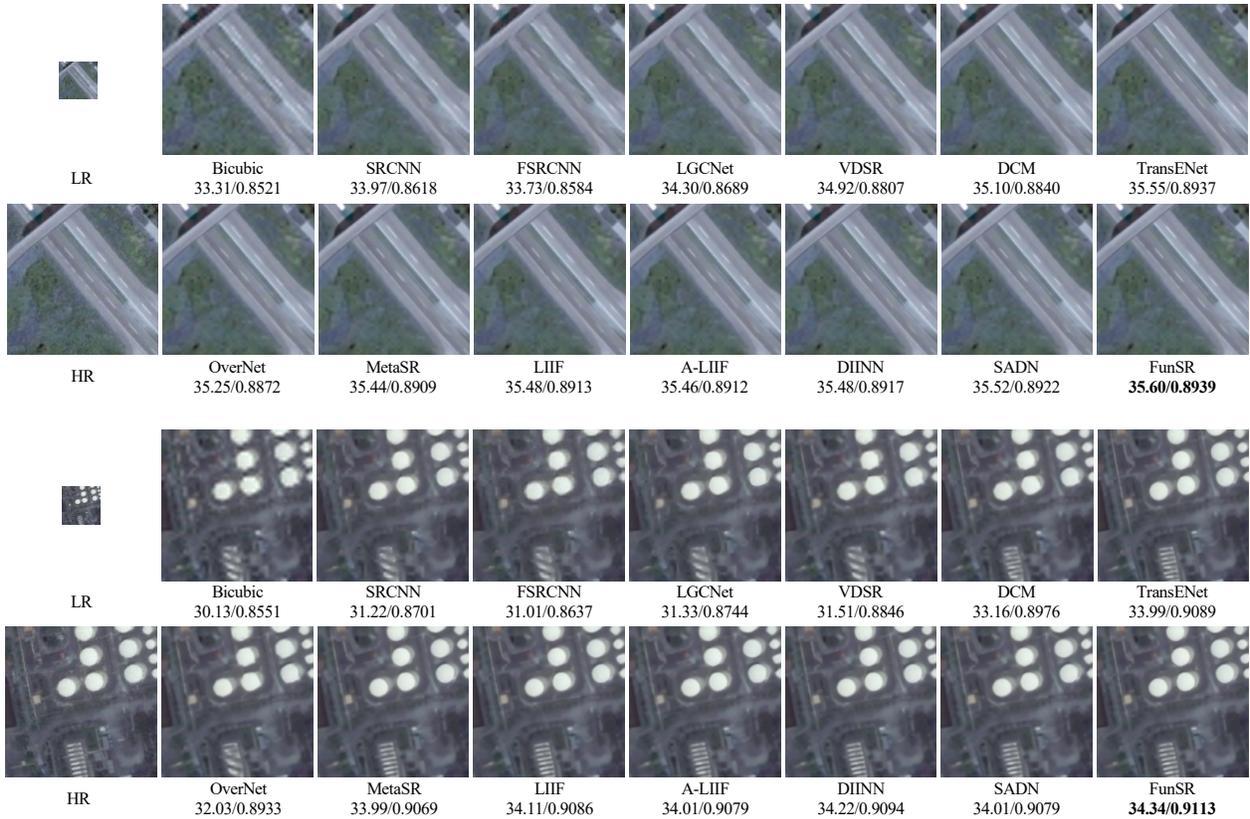

Fig. 8. Comparisons on the AID test set with different methods under ×4 factor. Image crops are from "viaduct_271" and "storagetanks_336" respectively. Zoom in for better visualization.

TABLE III
MEAN PSNR (DB) AND SSIM OF EACH SCENE CLASS ON THE UCMERCED TEST DATASET WITH THE UPSCALE FACTOR OF ×4.

class	Bicubic	SRCNN [64]	FSRCNN [65]	LGCNet [7]	VDSR [34]	DCM [36]	TransENet [41]
1	22.95/0.3882	23.55/0.4065	23.63/0.4239	24.06/0.4868	25.26/0.5739	26.17/0.6465	**26.91/0.6757**
2	24.07/0.7093	24.62/0.7324	24.31/0.7208	24.77/0.7403	25.26/0.7575	25.24/0.7563	26.08/0.7825
3	30.79/0.7901	31.69/0.8043	31.34/0.7988	31.81/0.8087	32.08/0.8166	32.11/0.8165	32.57/0.8271
4	30.98/0.8101	31.43/0.8125	31.23/0.8103	31.48/0.8160	31.58/0.8195	31.63/0.8203	32.28/**0.8449**
5	21.73/0.6908	22.28/0.7247	22.11/0.7160	22.39/0.7350	22.82/0.7543	22.83/0.7525	23.33/0.7743
6	23.29/0.6629	23.43/0.6576	23.38/0.6549	23.56/0.6688	23.78/0.6876	23.74/0.6838	24.30/**0.7189**
7	22.08/0.6731	22.74/0.7077	22.48/0.6937	22.92/0.7200	23.61/0.7472	23.55/0.7463	24.97/0.7964
8	26.28/0.6255	26.61/0.6225	26.54/0.6200	26.68/0.6283	26.99/0.6486	26.98/0.6492	27.41/0.6766
9	24.51/0.7085	25.40/0.7403	24.94/0.7225	25.74/0.7545	27.32/0.8000	27.68/0.8110	29.11/0.8502
10	29.43/0.7579	30.26/0.7737	29.80/0.7649	30.43/0.7794	30.84/0.7904	30.86/0.7924	31.53/**0.8096**
11	19.80/0.6932	20.53/0.7295	20.31/0.7198	20.70/0.7422	21.27/0.7684	21.52/0.7744	22.75/0.8181
12	24.31/0.7020	24.78/0.7138	24.61/0.7072	24.91/0.7205	25.34/0.7394	25.34/0.7408	26.27/0.7760
13	21.74/0.6102	22.21/0.6289	22.10/0.6235	22.33/0.6383	22.75/0.6592	22.69/0.6564	23.61/0.6941
14	22.57/0.7198	23.07/0.7420	22.82/0.7288	23.28/0.7516	23.99/0.7796	24.02/0.7776	25.31/0.8206
15	22.80/0.6744	23.64/0.7103	23.38/0.6960	23.94/0.7246	25.15/0.7737	25.53/0.7866	27.20/0.8328
16	19.06/0.6417	19.16/0.6505	19.06/0.6446	19.27/0.6630	19.82/0.6962	19.88/0.6931	21.72/0.7778
17	26.55/0.6757	27.34/0.6856	27.24/0.6840	27.46/0.6907	27.85/0.7051	27.82/0.7067	28.18/0.7248
18	26.98/0.7105	28.00/0.7321	27.45/0.7212	28.36/0.7415	28.96/0.7608	29.14/0.7625	30.72/0.7945
19	24.13/0.6050	24.51/0.6160	24.31/0.6110	24.62/0.6225	24.91/0.6375	24.93/0.6354	25.33/0.6532
20	25.00/0.7395	25.79/0.7667	25.52/0.7571	25.96/0.7763	26.64/0.7977	26.78/0.7995	27.99/0.8355
21	26.58/0.6973	27.04/0.7078	26.79/0.6993	27.16/0.7173	27.79/0.7513	27.95/0.7614	28.91/0.8014
Average	24.55/0.6803	25.15/0.6984	24.92/0.6913	25.33/0.7108	25.90/0.7364	26.02/0.7414	26.98/0.7755

class	OverNet [66]	MetaSR [47]	LIIF [32]	A-LIIF [67]	DIINN [68]	SADN [69]	FunSR
1	25.27/0.5752	26.01/0.6230	25.78/0.5886	25.25/0.5441	25.03/0.5609	24.76/0.5375	25.22/0.5659
2	25.38/0.7618	25.96/0.7763	26.09/0.7805	26.00/0.7774	26.32/0.7868	26.31/0.7851	**26.43/0.7892**
3	32.19/0.8186	32.57/0.8253	32.60/0.8257	32.55/0.8247	32.73/0.8286	32.66/0.8279	**32.74/0.8299**
4	31.66/0.8225	31.94/0.8299	32.04/0.8333	31.94/0.8304	32.15/0.8397	32.12/0.8380	**32.35**/0.8445
5	23.06/0.7631	23.53/0.7794	23.59/0.7821	23.47/0.7787	23.55/0.7846	23.58/0.7846	**23.87/0.7919**
6	23.75/0.6837	24.05/0.7014	24.13/0.7052	24.07/0.7018	24.18/0.7118	24.17/0.7103	**24.33**/0.7186
7	23.78/0.7572	24.61/0.7834	24.85/0.7913	24.62/0.7845	25.09/0.8000	25.00/0.7972	**25.39/0.8069**
8	26.90/0.6446	27.30/0.6657	27.33/0.6670	27.30/0.6651	27.38/0.6730	27.36/0.6722	**27.47/0.6767**
9	27.83/0.8169	28.74/0.8369	28.98/0.8419	28.63/0.8372	29.36/0.8542	29.17/0.8478	**29.66/0.8579**
10	30.83/0.7914	31.22/0.8011	31.29/0.8021	31.21/0.8008	31.43/0.8064	31.40/0.8060	**31.57**/0.8095
11	21.41/0.7754	22.57/0.8096	22.81/0.8166	22.61/0.8115	23.12/0.8261	23.01/0.8239	**23.45/0.8319**
12	25.55/0.7479	26.18/0.7723	26.35/0.7793	26.17/0.7724	26.53/0.7888	26.52/0.7857	**26.87/0.7966**
13	22.80/0.6631	23.42/0.6853	23.49/0.6879	23.39/0.6835	23.68/0.6981	23.62/0.6959	**23.89/0.7047**
14	24.23/0.7875	25.19/0.8153	25.36/0.8212	25.21/0.8172	25.59/0.8298	25.51/0.8273	**25.78/0.8336**
15	25.71/0.7928	27.12/0.8311	27.38/0.8361	27.11/0.8299	27.92/0.8476	27.66/0.8430	**28.21/0.8527**
16	19.72/0.6912	21.10/0.7536	21.38/0.7657	21.06/0.7539	21.92/0.7870	21.82/0.7837	**22.49/0.8048**
17	27.90/0.7074	28.21/0.7186	28.22/0.7187	28.22/0.7174	**28.33**/0.7233	28.31/0.7234	28.32/**0.7269**
18	29.18/0.7659	30.13/0.7837	30.33/0.7881	30.13/0.7829	30.72/0.7963	30.75/0.7948	**31.25/0.8009**
19	25.04/0.6382	25.38/0.6504	25.43/0.6512	25.35/0.6492	25.48/0.6573	25.40/0.6547	**25.57/0.6597**
20	26.98/0.8064	27.94/0.8302	28.05/0.8346	27.93/0.8304	28.43/0.8464	28.29/0.8429	**28.66/0.8508**
21	27.91/0.7547	28.90/0.7999	28.98/0.8034	28.89/0.7984	29.32/0.8165	29.22/0.8131	**29.55/0.8224**
Average	26.05/0.7412	26.76/0.7654	26.88/0.7676	26.72/0.7615	27.06/0.7744	26.98/0.7712	**27.29/0.7798**

continuous image SR algorithms over different backbones for in-distribution and out-of-distribution training magnifications.

The comprehensive results of various methods for all 21 scene classes[1] of the UCMeced dataset are available in Tab. III at ×4 magnification. We can see that FunSR achieves the best PSNR/SSIM values in most scene classes, whereas TransENet achieves comparable performance in the remaining four, namely agricultural, beach, chaparral, and golfcourse.

[1]All the 21 classes of the UCMerced dataset: 1 agricultural, 2 airplane, 3 baseballdiamond, 4 beach, 5 buildings, 6 chaparral, 7 denseresidential, 8 forest, 9 freeway, 10 golfcourse, 11 harbor, 12 intersection, 13 mediumresidential, 14 mobilehomepark, 15 overpass, 16 parkinglot, 17 river, 18 runway, 19 sparseresidential, 20 storagetanks, and 21 tenniscourt.

When compared to the TransENet, FunSR is more effective in situations with high-frequency characteristics and repetitive patterns, such as buildings, dense residences, storage tanks, and tennis courts.

2) Quantitative Results on AID Dataset: We conduct comparison experiments on the AID dataset to further validate FunSR's effectiveness. Unlike the UCMerced dataset, this one is larger in size and has more scene categories, totaling 30. Tab. II displays the overall results of various methods on this dataset. It can be seen that, when compared to other approaches, FunSR produces the best results on the majority of magnifications presented across different image encoders.

In addition, Tab. IV lists the detailed performance on the

TABLE IV
MEAN PSNR (DB) AND SSIM OF EACH SCENE CLASS ON THE AID TEST DATASET WITH THE UPSCALE FACTOR OF ×4.

class	Bicubic	SRCNN [64]	FSRCNN [65]	LGCNet [7]	VDSR [34]	DCM [36]	TransENet [41]
1	26.20/0.7252	26.96/0.7469	26.90/0.7433	27.21/0.7564	27.65/0.7740	27.87/0.7815	28.19/0.7942
2	34.91/0.8320	34.95/0.8327	34.70/0.8299	35.01/0.8342	35.26/0.8395	35.33/0.8402	35.18/0.8375
3	33.06/0.8443	33.92/0.8584	33.50/0.8526	34.20/0.8641	34.69/0.8728	34.82/0.8752	35.05/0.8787
4	31.42/0.7812	31.71/0.7886	31.53/0.7856	31.80/0.7917	32.11/0.7982	32.24/0.8004	32.26/0.8035
5	27.43/0.7576	28.58/0.7874	28.40/0.7827	29.20/0.8035	30.35/0.8358	30.67/0.8454	31.49/0.8624
6	26.16/0.7301	27.17/0.7626	26.99/0.7564	27.60/0.7767	28.47/0.7993	28.79/0.8092	29.54/0.8302
7	20.87/0.5550	21.91/0.6053	21.81/0.5972	22.30/0.6281	22.88/0.6580	23.15/0.6695	23.48/0.6957
8	24.67/0.7020	25.25/0.7216	25.21/0.7173	25.38/0.7284	25.73/0.7456	25.91/0.7514	26.13/0.7650
9	21.74/0.5905	22.32/0.6166	22.26/0.6105	22.45/0.6279	22.77/0.6496	22.94/0.6563	23.22/0.6827
10	36.54/0.8724	37.07/0.8792	36.79/0.8763	37.21/0.8821	37.28/0.8837	37.41/0.8866	37.32/0.8855
11	32.42/0.8119	33.33/0.8296	33.17/0.8264	33.68/0.8376	34.28/0.8518	34.58/0.8594	34.71/0.8633
12	26.77/0.6171	27.10/0.6154	27.04/0.6116	27.19/0.6199	27.39/0.6330	27.47/0.6348	27.46/0.6507
13	23.75/0.6569	24.66/0.6915	24.50/0.6840	25.02/0.7077	25.69/0.7379	26.00/0.7513	26.48/0.7790
14	32.40/0.7263	32.88/0.7386	32.78/0.7377	32.93/0.7423	33.09/0.7470	33.21/0.7483	33.15/0.7523
15	23.73/0.6017	24.47/0.6383	24.35/0.6331	24.70/0.6542	25.20/0.6789	25.37/0.6846	25.67/0.7043
16	27.22/0.6972	27.75/0.7065	27.68/0.7030	27.80/0.7097	27.89/0.7175	27.96/0.7187	27.89/0.7268
17	27.68/0.7320	28.32/0.7457	28.24/0.7411	28.42/0.7507	28.65/0.7604	28.68/0.7609	28.71/0.7695
18	21.30/0.6982	21.74/0.7250	21.61/0.7174	21.90/0.7363	22.56/0.7648	22.97/0.7797	24.36/0.8247
19	34.50/0.8506	35.27/0.8635	34.99/0.8588	35.56/0.8701	36.30/0.8824	36.55/0.8869	37.16/0.8953
20	36.30/0.8946	37.32/0.9029	36.93/0.9011	37.56/0.9062	37.87/0.9109	37.98/0.9125	38.01/0.9109
21	25.07/0.7859	25.83/0.8088	25.72/0.8038	26.07/0.8178	26.52/0.8322	26.80/0.8393	27.28/0.8546
22	24.72/0.6747	25.65/0.7152	25.54/0.7097	26.11/0.7374	27.04/0.7817	27.43/0.7998	28.12/0.8271
23	24.86/0.6935	25.33/0.7120	25.21/0.7053	25.49/0.7210	25.97/0.7399	26.13/0.7440	26.38/0.7605
24	28.96/0.7334	29.65/0.7454	29.54/0.7422	29.80/0.7507	30.00/0.7595	30.05/0.7599	30.06/0.7647
25	23.40/0.6653	24.09/0.6924	23.98/0.6838	24.29/0.7031	24.71/0.7237	24.91/0.7288	25.31/0.7504
26	22.68/0.5717	23.47/0.6086	23.41/0.6036	23.73/0.6229	24.11/0.6411	24.27/0.6442	24.43/0.6596
27	27.60/0.7451	28.19/0.7747	28.00/0.7671	28.45/0.7863	29.07/0.8049	29.22/0.8091	29.60/0.8254
28	30.47/0.8352	32.08/0.8570	31.83/0.8520	32.33/0.8618	32.95/0.8707	33.22/0.8762	34.02/0.8892
29	22.44/0.6372	23.40/0.6784	23.29/0.6713	23.72/0.6947	24.23/0.7199	24.52/0.7292	25.04/0.7514
30	24.96/0.6497	25.88/0.6865	25.76/0.6820	26.33/0.7091	27.18/0.7537	27.48/0.7684	28.11/0.7986
Average	27.48/0.7245	28.21/0.7465	28.06/0.7416	28.45/0.7563	28.93/0.7743	29.14/0.7804	29.47/0.7937

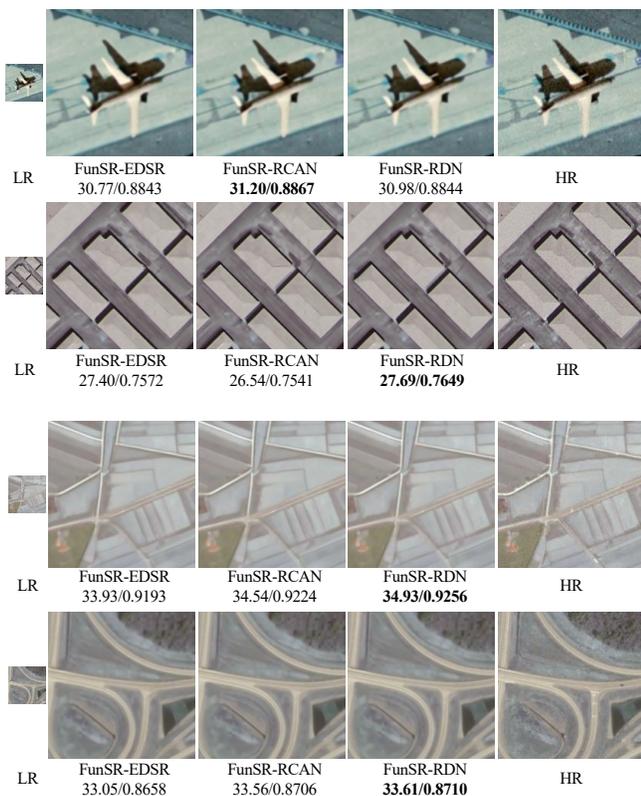| class	OverNet [66]	MetaSR [47]	LIIF [32]	A-LIIF [67]	DIINN [68]	SADN [69]	FunSR
1	27.96/0.7853	28.24/0.7950	28.31/0.7961	28.25/0.7947	28.42/0.7987	28.32/0.7960	**28.62/0.8037**
2	35.39/0.8411	35.43/0.8424	35.43/0.8429	35.41/0.8424	35.45/0.8434	35.43/0.8426	**35.51/0.8463**
3	34.87/0.8769	35.12/0.8815	35.15/0.8818	35.11/0.8812	35.22/0.8831	35.18/0.8825	**35.34/0.8872**
4	32.33/0.8027	32.43/0.8048	32.43/0.8054	32.42/0.8051	32.47/0.8065	32.43/0.8056	**32.56/0.8109**
5	30.93/0.8502	31.46/0.8619	31.49/0.8627	31.44/0.8615	31.63/0.8658	31.49/0.8629	**31.79/0.8692**
6	28.98/0.8123	29.59/0.8283	29.64/0.8314	29.56/0.8281	29.78/0.8354	29.63/0.8303	**30.04/0.8427**
7	23.31/0.6780	23.60/0.6920	23.62/0.6950	23.60/0.6923	23.74/0.7005	23.66/0.6966	**23.88/0.7077**
8	25.97/0.7552	26.24/0.7662	26.26/0.7672	26.21/0.7653	26.32/0.7695	26.26/0.7672	**26.44/0.7741**
9	23.06/0.6636	23.27/0.6754	23.31/0.6784	23.26/0.6757	23.36/0.6822	23.30/0.6789	**23.55/0.6903**
10	37.39/0.8860	37.48/0.8877	37.51/0.8884	37.50/0.8883	37.52/0.8885	37.50/0.8882	**37.72/0.8950**
11	34.65/0.8620	34.90/0.8673	34.92/0.8676	34.90/0.8670	34.97/0.8688	34.93/0.8679	**35.05/0.8721**
12	27.50/0.6394	27.61/0.6457	27.62/0.6482	27.60/0.6452	27.66/0.6519	27.64/0.6495	**27.72/0.6565**
13	26.16/0.7576	26.53/0.7741	26.55/0.7762	26.50/0.7731	26.65/0.7807	26.56/0.7763	**26.81/0.7869**
14	33.27/0.7518	33.35/0.7539	33.38/0.7551	33.33/0.7546	33.35/0.7555	33.36/0.7545	**33.45/0.7602**
15	25.48/0.6900	25.80/0.7014	25.84/0.7043	25.80/0.7025	25.90/0.7069	25.83/0.7055	**26.00/0.7124**
16	27.97/0.7213	28.06/0.7250	28.07/0.7255	28.06/0.7251	28.10/0.7272	28.08/0.7258	**28.19/0.7320**
17	28.74/0.7631	28.89/0.7689	28.91/0.7699	28.88/0.7689	28.95/0.7719	28.91/0.7702	**29.03/0.7762**
18	23.36/0.7927	24.24/0.8179	24.31/0.8203	24.20/0.8171	24.62/0.8280	24.36/0.8209	**24.94/0.8368**
19	36.85/0.8920	37.28/0.8992	37.30/0.8995	37.23/0.8987	37.43/0.9015	37.25/0.8989	**37.59/0.9056**
20	38.02/0.9129	38.18/0.9146	38.17/0.9147	38.15/0.9147	38.26/0.9156	38.17/0.9149	**38.33/0.9182**
21	26.89/0.8433	27.38/0.8545	27.39/0.8554	27.33/0.8541	27.48/0.8579	27.39/0.8562	**27.68/0.8636**
22	27.68/0.8091	28.19/0.8263	28.21/0.8265	28.13/0.8239	28.31/0.8300	28.20/0.8256	**28.48/0.8351**
23	26.26/0.7492	26.51/0.7588	26.55/0.7606	26.50/0.7589	26.64/0.7645	26.54/0.7611	**26.72/0.7682**
24	30.09/0.7624	30.22/0.7659	30.23/0.7670	30.22/0.7665	30.26/0.7680	30.23/0.7666	**30.33/0.7718**
25	25.07/0.7363	25.35/0.7471	25.41/0.7499	25.36/0.7475	25.47/0.7525	25.41/0.7504	**25.62/0.7585**
26	24.39/0.6501	24.61/0.6580	24.64/0.6604	24.61/0.6588	24.72/0.6637	24.66/0.6616	**24.80/0.6676**
27	29.42/0.8154	29.74/0.8258	29.81/0.8276	29.72/0.8255	29.86/0.8306	29.80/0.8272	**30.03/0.8354**
28	33.46/0.8813	33.99/0.8921	34.09/0.8930	33.94/0.8905	34.20/0.8944	33.99/0.8898	**34.53/0.9007**
29	24.60/0.7345	25.04/0.7488	25.08/0.7505	25.02/0.7481	25.16/0.7544	25.06/0.7507	**25.34/0.7598**
30	27.60/0.7737	28.12/0.7944	28.17/0.7966	28.10/0.7934	28.26/0.8005	28.17/0.7964	**28.39/0.8054**
Average	29.26/0.7850	29.57/0.7946	29.60/0.7960	29.55/0.7944	29.68/0.7987	29.60/0.7961	**29.82/0.8018**

Fig. 9. Some SR results on the UCMerced dataset (top two rows) and the AID dataset (bottom two rows) with different image encoders under the ×4 factor. Image crops are from "airplane15", "buildings25", "farmland_112", and "viaduct_108" respectively. Zoom in for better visualization.

30 classes[2] with a magnification of ×4. It demonstrates that FunSR delivers the best results on all the surface target scenes. According to Tab. II and Tab. IV, it implies that FunSR can produce better results as the quantity of the dataset and the complexity of the data expand.

3) Qualitative Visual Comparisons: In addition to quantitative comparison, we have presented some visual examples from FunSR-RDN on continuous magnification factors in Fig. 5. It can be observed that the proposed FunSR can be used to generate considerable visual effects in image SR at continuous magnification. For a better visual comparison with other methods, we here provide a qualitative comparison of the recovered results under the upscale factor of ×4. Fig. 7 displays some super-resolved examples of the UCMerced dataset including "parking lot" and "dense residential" scenes, while Fig. 8 presents some of the AID dataset, including "viaduct" and "storage tanks" scenes. Overall, when compared to other approaches, the proposed FunSR produces better results with crisper edges and contours that are also closer to the HR references.

[2]All the 30 classes of the AID dataset: 1 Airport, 2 BareLand, 3 Baseball-Field, 4 Beach, 5 Bridge, 6 Center, 7 Church, 8 Commercial, 9 DenseResidential, 10 Desert, 11 Farmland, 12 Forest, 13 Industrial, 14 Meadow, 15 MediumResidential, 16 Mountain, 17 Park, 18 Parking, 19 Playground, 20 Pond, 21 Port, 22 RailwayStation, 23 Resort, 24 River, 25 School, 26 SparseResidential, 27 Square, 28 Stadium, 29 StorageTanks, and 30 Viaduct.

TABLE V
ABLATION OF VARIOUS COMPONENTS IN FUNSR-EDSR. MEAN PSNR (DB) AND SSIM ON THE UC TEST DATASET WITH CONTINUOUS UPSCALE FACTORS ARE PROVIDED.

$\Phi_{pyramid}$	$\Phi_{interactor}$	Φ_{global}	×2.0	×2.5	×3.0	×3.5	×4.0
✓			34.01/0.9251	30.83/0.8759	28.61/0.8247	27.50/0.7946	26.46/0.7574
✓	✓		34.36/0.9279	31.15/0.8823	28.97/0.8365	27.86/0.8054	26.86/0.7733
✓	✓		34.49/0.9306	31.27/0.8847	29.10/0.8389	27.98/0.8077	26.95/0.7751
✓	✓	✓	**34.61/0.9318**	**31.40/0.8860**	**29.19/0.8391**	**28.10/0.8095**	**27.11/0.7781**

TABLE VI
ABLATION OF THE POSITIONAL ENCODING (PE) AND THE LEARNABLE GLOBAL TOKEN (LT) IN THE FUNCTIONAL INTERACTOR.

PE	LT	×2.0	×2.5	×3.0	×3.5	×4.0
✓		32.07/0.9024	28.91/0.8366	26.77/0.7731	25.64/0.7271	24.71/0.6855
	✓	34.28/0.9283	31.06/0.8825	28.98/0.8358	27.75/0.8047	26.75/0.7731
✓	✓	**34.61/0.9318**	**31.40/0.8860**	**29.19/0.8391**	**28.10/0.8095**	**27.11/0.7781**

TABLE VII
ABLATION OF DIFFERENT INPUT ATTRIBUTES (GC: GLOBAL COORDINATE, LC: LOCAL COORDINATE, SR: SCALE RATIO, RGB: INTERPOLATED RGB VALUE) IN THE FUNCTIONAL PARSER.

GC	LC	SR	RGB	×2.0	×2.5	×3.0	×3.5	×4.0
✓				33.97/0.9245	30.63/0.8709	28.52/0.8184	27.37/0.7877	26.43/0.7497
✓	✓			34.39/0.9292	31.03/0.8782	28.82/0.8271	27.71/0.7960	26.67/0.7601
✓	✓	✓		34.54/0.9317	31.17/0.8816	29.01/0.8308	27.87/0.7990	26.86/0.7657
✓	✓	✓	✓	**34.61/0.9318**	**31.40/0.8860**	**29.19/0.8391**	**28.10/0.8095**	**27.11/0.7781**

E. Ablation Study

In this section, we run a series of experiments on the UCMereced dataset to explore the significance of each component in our method, with all models trained with the same settings of the EDSR image encoder unless otherwise specified.

1) Effects of Different Components in FunSR: We conducted relevant ablation experiments with FunSR-EDSR on the UCMerced dataset to validate the effectiveness of components in the proposed FunSR. As seen in Tab. V, performance tends to grow monotonically with the increased component terms, from 26.46/0.7574 to 27.11/0.7781 on PSNR/SSIM metric under ×4 upscale factor, suggesting that all the designed components count. To intuitively depict the role of the local and the global parsers, Fig. 6 shows the final feature map (2 × 3 feature maps) generated by the two parsers. It can be seen that the global parser prioritizes the restoration of the overall scene, whereas the local parser pays more attention to details, such as contours, textures, etc.

2) Effects of Different Image Encoders in the Functional Representor: We have tried different image encoders on the LR images in the proposed FunSR to learn shallow functional representations. Tab. I and Tab. II display the performance values of different encoders on the two datasets respectively. Experiments show that FunSR can outperform other methods across different image encoders. Fig. 9 provides a straightforward visualization for comparing SR results among different image encoders.

3) Effects of Positional Encoding and Learnable Global Token in the Functional Interactor: The functional interactor is designed to allow each pixel-wise function to interact with functions in other locations, hence improving global semantic coherence. To actualize the interaction process, we use a Transformer-based design. We conducted ablation studies on
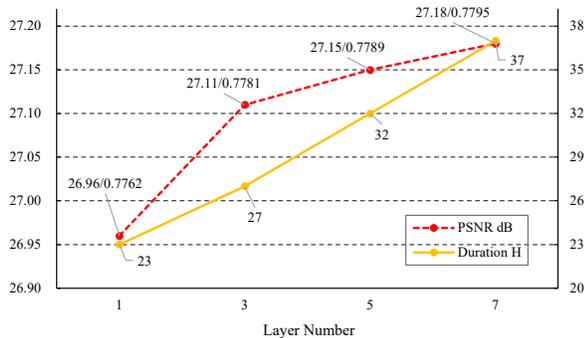
Fig. 10. PSNR/SSIM and convergence duration time over different layer numbers of the interactor.
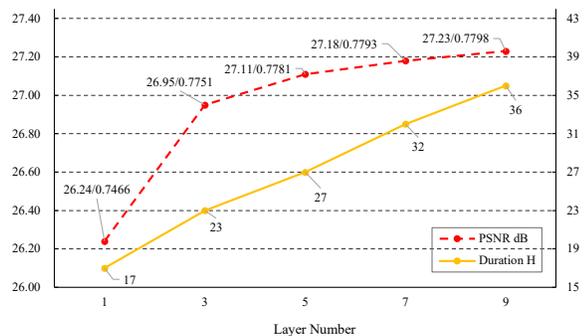

Fig. 11. PSNR/SSIM and convergence duration time over different layer numbers of the parser.

the positional encoding and the learnable global token to validate the necessity for its internal detailed designs. For the design without a learnable global token, we use a global pooling operation on the feature map generated by the interactor to form the global function parameters (θ_{global}). Tab. VI shows the ablation results on the UCMerced dataset using FunSR-EDSR. It indicates that FunSR performs significantly worse without the global learnable token and marginally worse without the positional encoding.

4) Effects of Different Input Attributes in the Functional Parser: The functional parser queries the pixel-wise functions based on the corresponding coordinates and parses the RGB pixel value of the position by inputting the global coordinates and certain extra properties, such as local coordinates, scale factor, and interpolated RGB value. Since it doesn't make sense to feed the local coordinates into the global parser, we only consider global coordinates in the global parser. Tab. VI indicates that as the input information increases, the SR performance also increases monotonically, *e.g.*, from 26.43/0.7497 to 27.11/0.7781 on PNSR/SSIM under the magnification of $\times 4$.

5) Layer Numbers of the Interactor and Parser: The layer numbers of the interactor and parser can have an effect on our method's performance. Therefore, we perform a series of experiments on this topic. In addition to the effectiveness metrics (PNSR and SSIM), we also pay attention to the efficiency, because the Transformer in the interactor and the MLP in the parser are resource consumption. Here we take the convergence duration time (H, Hour) during training to

measure the efficiency. We conduct the experiments on a single NVIDIA A100 Tensor Core GPU with a batch size of 8. Fig. 10 and Fig. 11 give a clear understanding of the PSNR/SSIM and convergence duration time over different layer numbers of the interactor and parser respectively. To balance efficiency and effectiveness, we finally choose a 3-layer interactor and a 5-layer parser to form the proposed FunSR.

V. CONCLUSION

In this paper, we propose FunSR, a novel SR framework for remote sensing images. FunSR aims at learning continuous representations for remote sensing images based on context interaction in implicit function space. It consists of three main parts: a functional representor, a functional interactor, and a functional parser. The representor first converts the LR image to a multi-scale continuous function representation, then the interactor allows each pixel-wise function to interact with functions at other locations and levels, and finally, the parser parses the discrete coordinates of the HR image to corresponding RGB values. The effectiveness of each component has been verified through ablation studies. Meanwhile, experimental results on two public datasets reveal that our method outperforms other state-of-the-art fixed magnification and continuous magnification methods in terms of super-resolved results.

REFERENCES

[1] D. Mahapatra, B. Bozorgtabar, and R. Garnavi, "Image super-resolution using progressive generative adversarial networks for medical image analysis," *Computerized Medical Imaging and Graphics*, vol. 71, pp. 30–39, 2019.

[2] Z. Chen, X. Guo, P. Y. Woo, and Y. Yuan, "Super-resolution enhanced medical image diagnosis with sample affinity interaction," *IEEE Transactions on Medical Imaging*, vol. 40, no. 5, pp. 1377–1389, 2021.

[3] Y. Pang, J. Cao, J. Wang, and J. Han, "Jcs-net: Joint classification and super-resolution network for small-scale pedestrian detection in surveillance images," *IEEE Transactions on Information Forensics and Security*, vol. 14, no. 12, pp. 3322–3331, 2019.

[4] L. Zhang, H. Zhang, H. Shen, and P. Li, "A super-resolution reconstruction algorithm for surveillance images," *Signal Processing*, vol. 90, no. 3, pp. 848–859, 2010.

[5] F. Liu, Q. Yu, L. Chen, G. Jeon, M. K. Albertini, and X. Yang, "Aerial image super-resolution based on deep recursive dense network for disaster area surveillance," *Personal and Ubiquitous Computing*, pp. 1–10, 2021.

[6] M. T. Merino and J. Nunez, "Super-resolution of remotely sensed images with variable-pixel linear reconstruction," *IEEE Transactions on Geoscience and Remote Sensing*, vol. 45, no. 5, pp. 1446–1457, 2007.

[7] S. Lei, Z. Shi, and Z. Zou, "Super-resolution for remote sensing images via local–global combined network," *IEEE Geoscience and Remote Sensing Letters*, vol. 14, no. 8, pp. 1243–1247, 2017.

[8] H. Ji, Z. Gao, T. Mei, and B. Ramesh, "Vehicle detection in remote sensing images leveraging on simultaneous super-resolution," *IEEE Geoscience and Remote Sensing Letters*, vol. 17, no. 4, pp. 676–680, 2019.

[9] L. Courtrai, M.-T. Pham, and S. Lefèvre, "Small object detection in remote sensing images based on super-resolution with auxiliary generative adversarial networks," *Remote Sensing*, vol. 12, no. 19, p. 3152, 2020.

[10] J. Xie, L. Fang, B. Zhang, J. Chanussot, and S. Li, "Super resolution guided deep network for land cover classification from remote sensing images," *IEEE Transactions on Geoscience and Remote Sensing*, vol. 60, pp. 1–12, 2021.

[11] J. Chen, K. Chen, H. Chen, Z. Zou, and Z. Shi, "A degraded reconstruction enhancement-based method for tiny ship detection in remote sensing images with a new large-scale dataset," *IEEE Transactions on Geoscience and Remote Sensing*, 2022.

[12] S. Lei, Z. Shi, X. Wu, B. Pan, X. Xu, and H. Hao, "Simultaneous super-resolution and segmentation for remote sensing images," in *IGARSS 2019-2019 IEEE International Geoscience and Remote Sensing Symposium*. IEEE, 2019, pp. 3121–3124.

[13] Q. Zhang, G. Yang, and G. Zhang, "Collaborative network for super-resolution and semantic segmentation of remote sensing images," *IEEE Transactions on Geoscience and Remote Sensing*, vol. 60, pp. 1–12, 2021.

[14] K. Chen, Z. Zou, and Z. Shi, "Building extraction from remote sensing images with sparse token transformers," *Remote Sensing*, vol. 13, no. 21, p. 4441, 2021.

[15] L. Chen, H. Liu, M. Yang, Y. Qian, Z. Xiao, and X. Zhong, "Remote sensing image super-resolution via residual aggregation and split attentional fusion network," *IEEE Journal of Selected Topics in Applied Earth Observations and Remote Sensing*, vol. 14, pp. 9546–9556, 2021.

[16] Z. Wang, J. Chen, and S. C. Hoi, "Deep learning for image super-resolution: A survey," *IEEE transactions on pattern analysis and machine intelligence*, vol. 43, no. 10, pp. 3365–3387, 2020.

[17] J. Xie, R. S. Feris, and M.-T. Sun, "Edge-guided single depth image super resolution," *IEEE Transactions on Image Processing*, vol. 25, no. 1, pp. 428–438, 2015.

[18] Y.-W. Tai, S. Liu, M. S. Brown, and S. Lin, "Super resolution using edge prior and single image detail synthesis," in *2010 IEEE computer society conference on computer vision and pattern recognition*. IEEE, 2010, pp. 2400–2407.

[19] J. Yang, J. Wright, T. S. Huang, and Y. Ma, "Image super-resolution via sparse representation," *IEEE transactions on image processing*, vol. 19, no. 11, pp. 2861–2873, 2010.

[20] J. Yang, J. Wright, T. Huang, and Y. Ma, "Image super-resolution as sparse representation of raw image patches," in *2008 IEEE conference on computer vision and pattern recognition*. IEEE, 2008, pp. 1–8.

[21] Y. Zhang, J. Liu, W. Yang, and Z. Guo, "Image super-resolution based on structure-modulated sparse represen-tation," *IEEE Transactions on Image Processing*, vol. 24, no. 9, pp. 2797–2810, 2015.

[22] H. Chang, D.-Y. Yeung, and Y. Xiong, "Super-resolution through neighbor embedding," in *Proceedings of the 2004 IEEE Computer Society Conference on Computer Vision and Pattern Recognition, 2004. CVPR 2004.*, vol. 1. IEEE, 2004, pp. I–I.

[23] T.-M. Chan, J. Zhang, J. Pu, and H. Huang, "Neighbor embedding based super-resolution algorithm through edge detection and feature selection," *Pattern Recognition Letters*, vol. 30, no. 5, pp. 494–502, 2009.

[24] J. Yamanaka, S. Kuwashima, and T. Kurita, "Fast and accurate image super resolution by deep cnn with skip connection and network in network," in *International Conference on Neural Information Processing*. Springer, 2017, pp. 217–225.

[25] C. Tian, R. Zhuge, Z. Wu, Y. Xu, W. Zuo, C. Chen, and C.-W. Lin, "Lightweight image super-resolution with enhanced cnn," *Knowledge-Based Systems*, vol. 205, p. 106235, 2020.

[26] C. Tian, Y. Xu, W. Zuo, B. Zhang, L. Fei, and C.-W. Lin, "Coarse-to-fine cnn for image super-resolution," *IEEE Transactions on Multimedia*, vol. 23, pp. 1489–1502, 2020.

[27] S. Lei and Z. Shi, "Hybrid-scale self-similarity exploitation for remote sensing image super-resolution," *IEEE Transactions on Geoscience and Remote Sensing*, vol. 60, pp. 1–10, 2021.

[28] M. Zhang and Q. Ling, "Supervised pixel-wise gan for face super-resolution," *IEEE Transactions on Multimedia*, vol. 23, pp. 1938–1950, 2020.

[29] Z. Wang, K. Jiang, P. Yi, Z. Han, and Z. He, "Ultra-dense gan for satellite imagery super-resolution," *Neurocomputing*, vol. 398, pp. 328–337, 2020.

[30] F. Yang, H. Yang, J. Fu, H. Lu, and B. Guo, "Learning texture transformer network for image super-resolution," in *Proceedings of the IEEE/CVF conference on computer vision and pattern recognition*, 2020, pp. 5791–5800.

[31] Z. Lu, J. Li, H. Liu, C. Huang, L. Zhang, and T. Zeng, "Transformer for single image super-resolution," in *Proceedings of the IEEE/CVF Conference on Computer Vision and Pattern Recognition*, 2022, pp. 457–466.

[32] Y. Chen, S. Liu, and X. Wang, "Learning continuous image representation with local implicit image function," in *Proceedings of the IEEE/CVF conference on computer vision and pattern recognition*, 2021, pp. 8628–8638.

[33] X. Xu, Z. Wang, and H. Shi, "Ultrasr: Spatial encoding is a missing key for implicit image function-based arbitrary-scale super-resolution," *arXiv preprint arXiv:2103.12716*, 2021.

[34] J. Kim, J. K. Lee, and K. M. Lee, "Accurate image super-resolution using very deep convolutional networks," in *Proceedings of the IEEE conference on computer vision and pattern recognition*, 2016, pp. 1646–1654.

[35] B. Lim, S. Son, H. Kim, S. Nah, and K. Mu Lee, "Enhanced deep residual networks for single image super-resolution," in *Proceedings of the IEEE conference on computer vision and pattern recognition workshops*,

2017, pp. 136–144.

[36] J. M. Haut, M. E. Paoletti, R. Fernandez-Beltran, J. Plaza, A. Plaza, and J. Li, "Remote sensing single-image super-resolution based on a deep compendium model," *IEEE Geoscience and Remote Sensing Letters*, vol. 16, no. 9, pp. 1432–1436, 2019.

[37] K. Simonyan and A. Zisserman, "Very deep convolutional networks for large-scale image recognition," *arXiv preprint arXiv:1409.1556*, 2014.

[38] Y. Zhang, Y. Tian, Y. Kong, B. Zhong, and Y. Fu, "Residual dense network for image super-resolution," in *Proceedings of the IEEE conference on computer vision and pattern recognition*, 2018, pp. 2472–2481.

[39] V. Sitzmann, J. Martel, A. Bergman, D. Lindell, and G. Wetzstein, "Implicit neural representations with periodic activation functions," *Advances in Neural Information Processing Systems*, vol. 33, pp. 7462–7473, 2020.

[40] K. Jiang, Z. Wang, P. Yi, G. Wang, T. Lu, and J. Jiang, "Edge-enhanced gan for remote sensing image superresolution," *IEEE Transactions on Geoscience and Remote Sensing*, vol. 57, no. 8, pp. 5799–5812, 2019.

[41] S. Lei, Z. Shi, and W. Mo, "Transformer-based multistage enhancement for remote sensing image super-resolution," *IEEE Transactions on Geoscience and Remote Sensing*, vol. 60, pp. 1–11, 2021.

[42] M. Qin, S. Mavromatis, L. Hu, F. Zhang, R. Liu, J. Sequeira, and Z. Du, "Remote sensing single-image resolution improvement using a deep gradient-aware network with image-specific enhancement," *Remote Sensing*, vol. 12, no. 5, p. 758, 2020.

[43] Z. Wang, L. Li, Y. Xue, C. Jiang, J. Wang, K. Sun, and H. Ma, "Fenet: Feature enhancement network for lightweight remote-sensing image super-resolution," *IEEE Transactions on Geoscience and Remote Sensing*, vol. 60, pp. 1–12, 2022.

[44] S. Lei, Z. Shi, and Z. Zou, "Coupled adversarial training for remote sensing image super-resolution," *IEEE Transactions on Geoscience and Remote Sensing*, vol. 58, no. 5, pp. 3633–3643, 2019.

[45] B. Liu, L. Zhao, J. Li, H. Zhao, W. Liu, Y. Li, Y. Wang, H. Chen, and W. Cao, "Saliency-guided remote sensing image super-resolution," *Remote Sensing*, vol. 13, no. 24, p. 5144, 2021.

[46] H. Shen, Z. Qiu, L. Yue, and L. Zhang, "Deep-learning-based super-resolution of video satellite imagery by the coupling of multiframe and single-frame models," *IEEE Transactions on Geoscience and Remote Sensing*, vol. 60, pp. 1–14, 2021.

[47] X. Hu, H. Mu, X. Zhang, Z. Wang, T. Tan, and J. Sun, "Meta-sr: A magnification-arbitrary network for super-resolution," in *Proceedings of the IEEE/CVF conference on computer vision and pattern recognition*, 2019, pp. 1575–1584.

[48] L. Wang, Y. Wang, Z. Lin, J. Yang, W. An, and Y. Guo, "Learning a single network for scale-arbitrary super-resolution," in *Proceedings of the IEEE/CVF international conference on computer vision*, 2021, pp. 4801–4810.

[49] N. Ni, H. Wu, and L. Zhang, "Hierarchical feature aggregation and self-learning network for remote sensing image continuous-scale super-resolution," *IEEE Geoscience and Remote Sensing Letters*, vol. 19, pp. 1–5, 2021.

[50] Y. Fu, J. Chen, T. Zhang, and Y. Lin, "Residual scale attention network for arbitrary scale image super-resolution," *Neurocomputing*, vol. 427, pp. 201–211, 2021.

[51] Y.-T. Liu, Y.-C. Guo, and S.-H. Zhang, "Enhancing multi-scale implicit learning in image super-resolution with integrated positional encoding," *arXiv preprint arXiv:2112.05756*, 2021.

[52] A. Vaswani, N. Shazeer, N. Parmar, J. Uszkoreit, L. Jones, A. N. Gomez, Ł. Kaiser, and I. Polosukhin, "Attention is all you need," *Advances in neural information processing systems*, vol. 30, 2017.

[53] A. Dosovitskiy, L. Beyer, A. Kolesnikov, D. Weissenborn, X. Zhai, T. Unterthiner, M. Dehghani, M. Minderer, G. Heigold, S. Gelly *et al.*, "An image is worth 16x16 words: Transformers for image recognition at scale," *arXiv preprint arXiv:2010.11929*, 2020.

[54] N. Carion, F. Massa, G. Synnaeve, N. Usunier, A. Kirillov, and S. Zagoruyko, "End-to-end object detection with transformers," in *European conference on computer vision*. Springer, 2020, pp. 213–229.

[55] Y. Zhang, K. Li, K. Li, L. Wang, B. Zhong, and Y. Fu, "Image super-resolution using very deep residual channel attention networks," in *Proceedings of the European conference on computer vision (ECCV)*, 2018, pp. 286–301.

[56] C.-Y. Wang, H.-Y. M. Liao, Y.-H. Wu, P.-Y. Chen, J.-W. Hsieh, and I.-H. Yeh, "Cspnet: A new backbone that can enhance learning capability of cnn," in *Proceedings of the IEEE/CVF conference on computer vision and pattern recognition workshops*, 2020, pp. 390–391.

[57] A. Bochkovskiy, C.-Y. Wang, and H.-Y. M. Liao, "Yolov4: Optimal speed and accuracy of object detection," *arXiv preprint arXiv:2004.10934*, 2020.

[58] M. Tancik, P. Srinivasan, B. Mildenhall, S. Fridovich-Keil, N. Raghavan, U. Singhal, R. Ramamoorthi, J. Barron, and R. Ng, "Fourier features let networks learn high frequency functions in low dimensional domains," *Advances in Neural Information Processing Systems*, vol. 33, pp. 7537–7547, 2020.

[59] B. Mildenhall, P. P. Srinivasan, M. Tancik, J. T. Barron, R. Ramamoorthi, and R. Ng, "Nerf: Representing scenes as neural radiance fields for view synthesis," *Communications of the ACM*, vol. 65, no. 1, pp. 99–106, 2021.

[60] K. Chen, W. Li, J. Chen, Z. Zou, and Z. Shi, "Resolution-agnostic remote sensing scene classification with implicit neural representations," *IEEE Geoscience and Remote Sensing Letters*, 2022.

[61] Y. Yang and S. Newsam, "Bag-of-visual-words and spatial extensions for land-use classification," in *Proceedings of the 18th SIGSPATIAL international conference on advances in geographic information systems*, 2010, pp. 270–279.

[62] G.-S. Xia, J. Hu, F. Hu, B. Shi, X. Bai, Y. Zhong,

L. Zhang, and X. Lu, "Aid: A benchmark data set for performance evaluation of aerial scene classification," *IEEE Transactions on Geoscience and Remote Sensing*, vol. 55, no. 7, pp. 3965–3981, 2017.

[63] Z. Wang, A. C. Bovik, H. R. Sheikh, and E. P. Simoncelli, "Image quality assessment: from error visibility to structural similarity," *IEEE transactions on image processing*, vol. 13, no. 4, pp. 600–612, 2004.

[64] C. Dong, C. C. Loy, K. He, and X. Tang, "Image super-resolution using deep convolutional networks," *IEEE transactions on pattern analysis and machine intelligence*, vol. 38, no. 2, pp. 295–307, 2015.

[65] C. Dong, C. C. Loy, and X. Tang, "Accelerating the super-resolution convolutional neural network," in *European conference on computer vision*. Springer, 2016, pp. 391–407.

[66] P. Behjati, P. Rodriguez, A. Mehri, I. Hupont, C. F. Tena, and J. Gonzalez, "Overnet: Lightweight multi-scale super-resolution with overscaling network," in *Proceedings of the IEEE/CVF Winter Conference on Applications of Computer Vision*, 2021, pp. 2694–2703.

[67] H. Li, T. Dai, Y. Li, X. Zou, and S.-T. Xia, "Adaptive local implicit image function for arbitrary-scale super-resolution," in *2022 IEEE International Conference on Image Processing (ICIP)*. IEEE, 2022, pp. 4033–4037.

[68] Q. H. Nguyen and W. J. Beksi, "Single image super-resolution via a dual interactive implicit neural network," in *Proceedings of the IEEE/CVF Winter Conference on Applications of Computer Vision*, 2023, pp. 4936–4945.

[69] H. Wu, N. Ni, and L. Zhang, "Scale-aware dynamic network for continuous-scale super-resolution," *arXiv preprint arXiv:2110.15655*, 2021.

[70] I. Loshchilov and F. Hutter, "Sgdr: Stochastic gradient descent with warm restarts," *arXiv preprint arXiv:1608.03983*, 2016.